Evolution of bottom boundary layers on three dimensional topography – Buoyancy adjustment and instabilities

Arjun Jagannathan [1]*, Kaushik Srinivasan [1], James C. McWilliams [1], Jeroen Molemaker [1], Andrew L. Stewart [1]

[1]Department of Atmospheric and Oceanic Sciences, University of California, Los Angeles, CA 90024, USA

Key Points:

- A complex interplay of buoyancy adjustment, instabilities, and curvature effects influences oceanic bottom bounday layers (BBL) evolution.
- Nonlinear strain effects contribute significantly in weakening the bottom stress during the initial current-ridge encounter.
- The onset of negative potential vorticity (NPV), and barotropic instabilities downstream partially offsets the reduced boundary dissipation.

*Current address, Indian Institute of Technology Madras, Chennai 600036, India

Corresponding author: Arjun Jagannathan, arjunj@iitm.ac.in

Abstract

A current along a sloping bottom gives rise to upwelling, or downwelling Ekman transport within the stratified bottom boundary layer (BBL), also known as the bottom Ekman layer. In 1D models of slope currents, geostrophic vertical shear resulting from horizontal buoyancy gradients within the BBL is predicted to eventually bring the bottom stress to zero, leading to a shutdown, or 'arrest ', of the BBL. Using 3D ROMS simulations, we explore how the dynamics of buoyancy adjustment in a current-ridge encounter problem differs from 1D and 2D temporal spin up problems. We show that in a downwelling BBL, the destruction of the ageostrophic BBL shear, and hence the bottom stress, is accomplished primarily by nonlinear straining effects during the initial topographic encounter. As the current advects along the ridge slopes, the BBL deepens and evolves toward thermal wind balance. The onset of negative potential vorticity (NPV) modes of instability and their subsequent dissipation partially offsets the reduction of the BBL dissipation during the ridge-current interaction. On the upwelling side, although the bottom stress weakens substantially during the encounter, the BBL experiences a horizontal inflectional point instability and separates from the slopes before sustained along-slope stress reduction can occur. In all our solutions, both the upwelling and downwelling BBLs are in a partially arrested state when the current separates from the ridge slope, characterized by a reduced, but non-zero bottom stress on the slopes.

Plain Language Summary

Surface winds pump mechanical energy into the large-scale circulation of the ocean at an average rate of between 0.8 TW and 1 TW. This wind-input occurs at large, so-called synoptic scales spanning thousands of kilometers. Absent dissipative pathways, this steady energy input would cause uncontrolled spinup of the ocean gyres. For decades it has been assumed that friction at the seabed has an important role in the eventual turbulent dissipation of the ocean kinetic energy. In the 1990s, theoretical models suggested that turbulence could be wholly suppressed on sloping bottom bathymetry due to the rearrangement of density surfaces within the bottom boundary layer — a mechanism called buoyancy adjustment. Here we revisit this problem using modern 3D simulations of currents encountering a ridge. We find that although the bottom stress can be markedly reduced on topographic slopes, the mechanism through which it occurs is quite different than that in simplified 1D and 2D models. Flow 'deformation ', or straining effects during the topographic encounter play a more important role in weakening the bottom stress than buoyancy adjustment. Furthermore, geometric effects like curvature, and flow instabilities

can partially offset the reduction in dissipation caused by suppression of bottom boundary layer turbulence.

1 Introduction

When a bottom boundary layer (BBL) develops over sloping bathymetry, buoyancy advection in the cross-slope direction produces horizontal buoyancy gradients within the BBL, and hence a geostrophic vertical shear through the thermal wind balance. This process, known as buoyancy adjustment (or Ekman adjustment), acts to oppose the ageostrophic boundary layer shear, thereby weakening the bottom stress on the slopes. In simplified models of slope currents (MacCready & Rhines, 1991; Garrett et al., 1993), a steady state is eventually reached in which the bottom stress collapses, bringing the cross slope Ekman transport to zero — a state referred to in the literature as 'Ekman arrest'. These predictions have been validated in 1D numerical models (Brink & Lentz, 2010a), but questions remain about their relevance to the real ocean.

Ekman pumping/suction resulting from the horizontal divergence of the Ekman transport is thought to be the primary mechanism behind the spin-down of interior flows in the ocean (Garrett et al., 1993). The drag exerted at the seafloor is also estimated to be an important source of energy dissipation (Wunsch & Ferrari, 2004; Sen et al., 2008). Reduced bottom stress and weakening turbulence in sloping BBLs could therefore have profound implications for our understanding of the global oceanic circulation and energy budget (Ruan, Wenegrat, & Gula, 2021). Umlauf et al. (2015) developed a theoretical framework to understand the energetic pathways during the process of Ekman arrest in a 1D BBL, which they then validated using simulations with a second order turbulence closure model. An interesting finding was that buoyancy adjustment in a BBL is very effective at converting the kinetic energy of the along-slope flow to available potential energy. In particular, for a downwelling (upwelling) BBL, the amount of energy stored as available potential energy after Ekman arrest (defined by the authors as bottom stress reducing below a threshold value) is as large as 40% (70%) of the energy lost to dissipation during the active adjustment process. Crucially, this means that during relaxation from an arrested state, this available potential energy stored in the BBL can be converted to turbulent kinetic energy and eventually dissipated. The implication is that the observation of a partially arrested BBL in some region along the seafloor does not preclude the same region from being a hotspot of dissipation in a different time window.

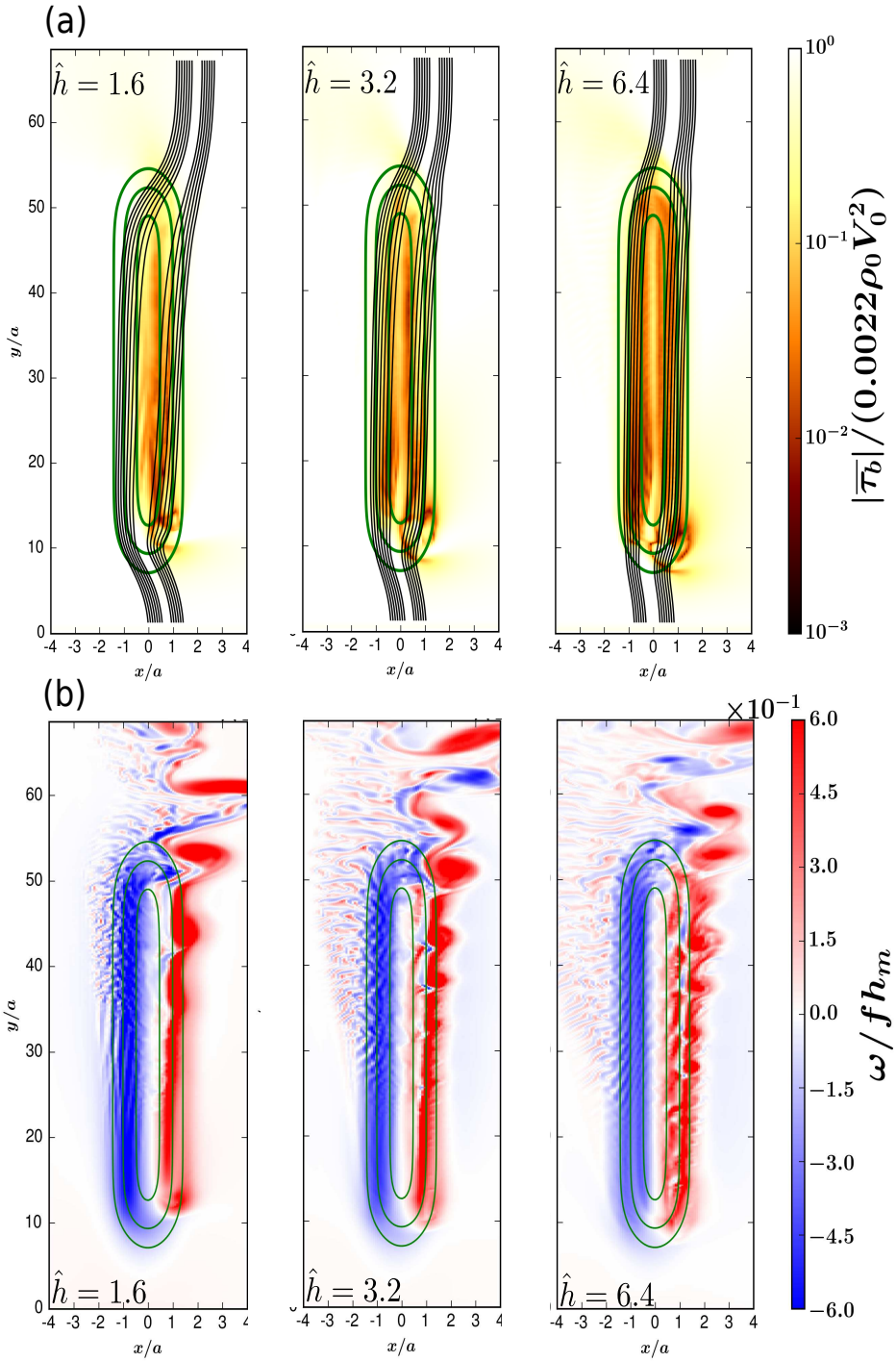

Figure 1. (Adapted from Figs. 1, 4 of Jagannathan et al., 2021, © American Meterological Society. Used with permission.) Encounter of a barotropic inflow with an elongated racetrack shaped ridge. Green lines are bathymetric contours at $z = 0.14h_m$, $z = 0.37h_m$ and $z = 0.9h_m$. The inflow is from south to north. (a) Normalized, time-averaged boundary stress $|\overline{\boldsymbol{\tau_b}}|/(C_d^*\rho_0 V_0^2)$, with a value $C_d^* = 0.0022$ (Sen et al., 2008; Arbic et al., 2009), along with selected barotropic streamlines (in black). Dark colors indicate stress reduction. Note that the colormap is saturated at 10^{-1}. (b) Instantaneous snapshots of normalized depth integrated vorticity ω (Eq. (5)). Small scale NPV instabilities are visible as banded patterns of vorticity on the anticyclonic side. Values of the parameter $\hat{h}$ are indicated inside each panel. Observe that the instability is trigerred further and further upstream for increasing $\hat{h}$ (Note: The vortices appear distorted as the figure is not to scale)

Some of the best available observational evidence for reduced bottom stress, or 'partial arrest ' over topography is described in Lentz and Trowbridge (2001). These authors analyzed moored current observations in the Northern California mid-shelf during the fall/winter period in 5 different years between 1981 and 1991. Among their findings is that isopycnals slope downward near the bottom and that the flow is close to a state of thermal wind balance throughout the water column. The near-bottom along-shelf currents, and hence bottom stress are thus found to be substantially weakened.

Complete Ekman arrest nevertheless remains elusive in oceanic observations of the BBL (Armi & Millard Jr, 1976; Armi, 1978; Armi & D'Asaro, 1980). Some recent studies provide clues on why this may be the case. Using LES simulations with doubly periodic boundary conditions in the cross- and along-slope directions, Ruan et al. (2019) showed that the BBL always relaminarizes before Ekman arrest can be achieved. The relaminarization, or turbulence collapse, in their solutions is clearly evident in Hovmöller diagrams that show negligible TKE within the BBL at later times (Fig. 12 in Ruan et al. (2019) and Fig. 6 in Ruan, Thompson, and Taylor (2021)). Once the BBL relaminarizes, subsequent evolution toward an arrested state can only proceed via non-turbulent molecular mixing, which is a relatively slow process. Wenegrat and Thomas (2020) further demonstrate how the arrest process can be delayed due to the onset of negative potential vorticity (NPV) instabilities.

To date, most numerical studies on Ekman arrest have focussed on the temporal adjustment problem in 1D (e.g. Brink & Lentz, 2010a, 2010b) and more recently, periodic 2D domains (e.g. Ruan et al., 2019; Wenegrat & Thomas, 2020). However, in the real ocean, buoyancy adjustment, be it on continental shelf slopes or isolated islands, follows a spatio-temporal evolution in the along-slope direction. Moreover it does not happen in isolation and is often intertwined with other processes like topographic vorticity generation, waves, and instabilities. Vorticity generation during flow past topography can occur purely through vortex tilting and stretching effects in the absence of either bottom drag or background rotation (Smolarkiewicz & Rotunno, 1989; Jagannathan et al., 2019). However Jagannathan et al. (2021) noted that drag-mediated vorticity generation is substantially more robust, generating larger and more energetic vortices. A flurry of recent computational studies have uncovered a rich panoply of vortical structures and associated energy exchanges that emerge in three dimensional, rotating, stratified topographic wakes, both with (Puthan et al., 2022b, 2022a), and without (Perfect et al., 2018, 2020a, 2020b; Srinivasan et al., 2019, 2021), tidal forcing. A notable finding in Perfect et al. (2018) is that in the limit of weak rotation, the vortex shedding frequency on the seamount slopes varies with depth, which leads to the emer-

gence of vertically decoupled vortical wakes —- a phenomenon also noticed by Srinivasan et al. (2021) in their simulations of equatorial wakes. Recent observational studies on topographically generated wakes in the Palau island chain (MacKinnon et al., 2019; St. Laurent et al., 2019; Zeiden et al., 2022) also reinforce the emerging understanding that eddying wakes are an important conduit in the oceanic turbulence cascade from the mesoscale to the dissipative microscales.

In the present work we analyze a set of idealized numerical simulations to examine how buoyancy adjustment evolves in a 3D slope-current encounter. This is a follow-up study to an earlier paper (Jagannathan et al., 2021) in which the primary focus was on elucidating the mechanism of vertical vorticity generation during the interaction of a boundary current with a topographic ridge. A key finding there was that much of the irreversible vertical vorticity is generated during the early encounter of the flow with the ridge, through the so-called bottom stress divergence torque (BSDT). The simulations analyzed here are those described in Jagannathan et al. (2021) along with an additional set of simulations in which we vary the ridge curvature in the along-slope direction.

In the following sections we describe the numerical model setup, analyze the buoyancy adjustment and BBL evolution in our solutions, along with its energetics, and discuss these results in the context of 1D and 2D theories of Ekman arrest on a slope.

2 Numerical setup

2.1 Basic model configuration

The simulations are performed using the Regional Ocean Modelling System (ROMS) (Shchepetkin & McWilliams, 2003), a terrain following model that solves the Boussinesq primitive equations under the hydrostatic approximation. The flow configuration is identical to that described in Jagannathan et al. (2021). For the sake of brevity, we confine our description here to the most essential aspects of the setup and refer the reader to Jagannathan et al. (2021) for further details.

A uniform barotropic inflow in the y direction, with speed

$$V_0(x, y = 0, z) = 0.105\,\mathrm{ms}^{-1} \tag{1}$$

and approximately uniform stratification N is incident on a ridge of height h_m and half-width a. The ridge is elongated in the y direction, with bathymetry contours resembling a racetrack (Fig.

1). The ridge height from the bottom is given by,

$$h = h_m e^{-x^2/a^2} \left[\frac{1+\tanh\left(\frac{y-y_1}{\sigma_y}\right)}{2} \right] \left[\frac{1+\tanh\left(\frac{y_2-y}{\sigma_y}\right)}{2} \right]. \tag{2}$$

In all our simulations the ridge height $h_m = 400$ m and its half-width $a = 3.5$ km. The length of the ridge is fixed at $y_2 - y_1 = 144$ km and the extent of the initial adjustment region over which the ridge elevation increases to h_m is given by $\sigma_y = 12$ km. The critical dimensionless parameter (Srinivasan et al., 2019; Jagannathan et al., 2021) is the non-dimensional height

$$\hat{h} = \frac{N h_m}{f a}, \tag{3}$$

where f is the Coriolis frequency. In the Ekman arrest literature where the slope $\tan\theta$ is typically chosen to be constant, the slope Burger number is defined as

$$Bu = N \tan\theta / f \approx N\theta / f, \tag{4}$$

for $\theta \ll 1$ (Brink & Lentz, 2010a; Wenegrat & Thomas, 2020). The parameter $\hat{h}$ in our simulations may thus be regarded as analogous to a slope Burger number, with $\theta = h_m/a$ being an average measure of the varying topographic slope.

Fig. 1 depicts the basic flow and ridge configuration along with maps of the time-averaged, normalized bottom stress $\boldsymbol{\tau}_b$ (Fig. 1a) and instantaneous snapshots of the depth integrated relative vertical vorticity (Fig. 1b), defined as

$$\omega = \int_{-H}^{-H+D} \zeta \, \mathrm{d}z, \tag{5}$$

for three different values of $\hat{h}$. In Eq. (5), $\zeta = (\partial v/\partial x - \partial u/\partial y)$ is the relative vertical vorticity while D is the local water column height. In all the simulations, the water depth $H = 1000$ m. The elongated ridge is well-suited to explore buoyancy adjustment amidst the full complexity of 3D motions including ageostrophic NPV instabilities (Wang et al., 2014), vorticity generation, flow separation and secondary circulations.

To investigate the effect of ridge curvature on the dynamics, we additionally consider an elliptical shaped ridge, with varying aspect ratio $\beta = b/a$, where b is the half-length,

$$h = h_m e^{-\left(\frac{x^2}{a^2}+\frac{y^2}{b^2}\right)}. \tag{6}$$

The ridge is centered in a computational domain that is 240 km long and 90 km wide. A zero-gradient condition is imposed on the barotropic (vertically-averaged) component of velocity and potential temperature at the lateral and outflow boundaries, while the Orlanski radiation condition (Orlanski, 1976) is specified for the baroclinic component.

2.2 Buoyancy adjustment on finite ridges with varying topographic slope

Compared to earlier 1D and 2D solutions of buoyancy adjustment on slope, our setup has two significant novelties. One is the non-constant slope and the other is the three dimensionality which introduces the possibility of flow separation, topographic waves and secondary horizontal circulations. To more precisely isolate the 3D effects, one may be tempted to separately consider the non-constant slope problem in 2D before attacking the 3D problem. However in practice we found that it is challenging to maintain a steady barotropic forcing in ROMS for the 2D slope current configuration. To see why this is the case, recall that the flow is initialized with a constant sea-surface gradient that geostrophically balances a barotropic inflow (Jagannathan et al., 2021). In 3D, specifying the sea surface height at the inflow boundary *and* the lateral boundaries is found to be sufficient to maintain a steady barotropic velocity everywhere downstream. However in the 2D configuration, once the flow is initialized, the only way to hold the barotropic inflow fixed as the flow evolves is by nudging either the sea surface height or the barotropic velocity itself. Both of these represent strong external forcing of the flow and introduce artefacts to the solution. For this reason, we directly consider the more realistic 3D problem without imposing any artificial constraints on the evolution of the along-slope flow.

The long straight section of the elongated ridge helps to isolate the buoyancy adjustment process and facilitates comparison with 1D and 2D model predictions. We examine in this study, solutions with $\hat{h} = 1.6, 3.2, 6.4$ and 12.8. Previous studies on buoyancy adjustment have focused predominantly on the parameter space $0 < \hat{h} < 2$, a range that is typical of many continental slopes. However there are many locations in the ocean where larger slope Burger numbers are common. An example of an isolated island where $\hat{h} \gg 1$ is Green island off Taiwan for which, substituting the values $h_m = 500$ m, $a = 3.5$ km (Fig. 1c of Chang et al., 2013), $f = 5.5 \times 10^{-5}\,\mathrm{s}^{-1}$ and a representative value for the buoyancy frequency squared $N^2 \approx 10^{-4}\,\mathrm{s}^{-2}$ (Fig. 5 of Hsu et al., 2019) gives $\hat{h} \approx 26$. Another site is the Florida straits in the stretch prior to when the Gulf Stream separates (Gula et al., 2015). Here the slope angle is as high as 3°. Using a mid-latitude value of $f = 7 \times 10^{-5}\,\mathrm{s}^{-1}$ and typical thermocline stratification $N \approx 10^{-2}\,s^{-1}$ then gives $\hat{h} \approx 7.5$. Recently, Nagai et al. (2021) note that in the Tokara strait, the Kuroshio flows past several steep seamounts where $\hat{h} \approx 3$. Moreover turbulence microstructure measurements above the sloping sides of these seamounts revealed 100-1000 fold enhancement of turbulent dissipation rates relative to typical open ocean values of $\mathscr{O}(10^{-10})\,\mathrm{Wkg}^{-1}$, which raises questions about the relative importance of buoyancy adjustment and eddying dynamics in sloping BBLs. Similar levels of enhancement in

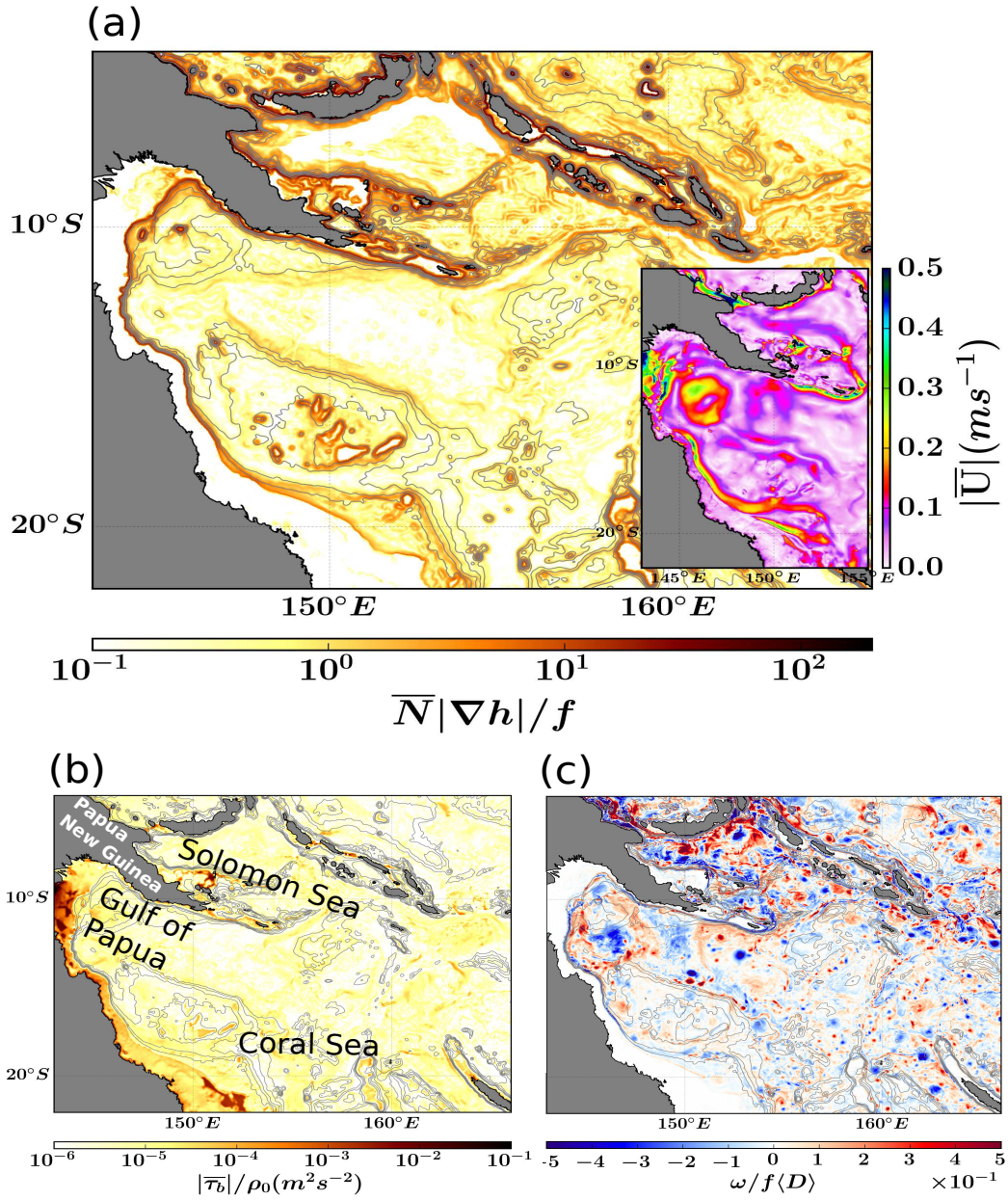

Figure 2. Three-month averages of local slope Burger number and bottom stress from a 1.5 km horizontal resolution solution of the Southwestern Pacific, over the winter months April-June. Bathymetry is contoured every 500 m and is indicated by dark gray lines. (a) Local slope Burger numbers $\overline{N}|\nabla h|/f$ where $|\nabla h|$ is the absolute value of the bathymetric gradient. The inset highlights the absolute value of the barotropic flow field $|\overline{\boldsymbol{U}}|$. (b) Bottom stress divided by the reference density $|\overline{\boldsymbol{\tau_b}}|/\rho_0)(m^2s^{-2})$. (c) Instantaneous snapshot of the depth integrated relative vertical vorticity, normalized by $f\langle D\rangle$, where $\langle D\rangle$ is the area-averaged water column height in the region, excluding the land regions.

the turbulent dissipation rate have been reported over the extremely steep slope angles (up to 35°) in the northern end of the Palau island chain (MacKinnon et al., 2019).

Our study in particular, is motivated by recent ROMS solutions of the Gulf of Papua and Solomon sea regions in the southwestern Pacific (Srinivasan et al., 2017). A spatial map of the three month averaged slope Burger number $\overline{N}|\nabla h|/f$ over the winter months of April-June (Fig. 2a) reveals extensive sections both along the continental slope and the island chains of Solomon and Vanuatu where the local slope Burger number ranges from $\mathcal{O}(1) - \mathcal{O}(10)$. Note that $|\nabla h|$ here denotes the absolute value of the local bathymetric slope and $\overline{N}$ is the three month averaged background stratification outside the BBL. The inset to Fig. 2a shows the three month averaged barotropic flow speed of the North Queensland current (which then turns easteward in the Gulf of Papua) as it flows along the continental shelf slope between 20°S and 10°S. Fig. 2b shows the bottom stress weakening between 20°S and 15° as the Gulf of Papua current navigates the sloping bathymetric region. The slope-current interaction also leads to the generation of anticyclonic vorticity on the slopes. Indeed a rich submesoscale eddy field comprising both cyclones and anticyclones is seen in instantaneous snapshots (Fig. 2c) of the depth integrated vorticity ω. Lastly, it is worthwhile to note that the bottom Ekman layer along the North Queensland current is downwelling favorable, which makes the BBL here a strong candidate for NPV instabilities. Thus the submesoscale flow in this region is endowed with many intriguing dynamical possibilities that idealized process studies can yield more insight about.

As described in Jagannathan et al. (2021), $\hat{h}$ in our simulations is varied by changing the stratification N while keeping the other parameters unchanged. The Coriolis frequency f is fixed at a value of $7 \times 10^{-5}\,\mathrm{s}^{-1}$ and N ranges from $1 \times 10^{-3}\,\mathrm{s}^{-1}$ in the $\hat{h} = 1.6$ run to $8 \times 10^{-3}\,\mathrm{s}^{-1}$ in the $\hat{h} = 12.8$ run. For the elliptical ridge, $\hat{h}$ is fixed at 3.2 and the semi-major length b is varied between 3.5 km and 56 km, so that the ellipse aspect ratio β spans values ranging from 1 to 16.

2.3 Bottom stress parameterization and grid resolution

The bottom stress in ROMS is parameterized using the quadratic drag law

$$\boldsymbol{\tau}_b = \rho_0 C_d \boldsymbol{u}_b ||\boldsymbol{u}_b||. \tag{7}$$

where ρ_0 is the constant reference density, $\boldsymbol{u}_b$ is the velocity in the bottommost σ layer and C_d is the drag constant

$$C_d = [\kappa / log(\Delta z_b / z_{ob})]^2. \tag{8}$$

$\kappa = 0.4$ in Eq. (8) is the Von-Karman constant, Δz_b is the thickness of the bottommost σ-layer and z_{ob} is the roughness length which we set to 1 cm. Substituting these parameters in Eq. (8), along with the observed range of values of Δz_b in our runs of 0.9-1.1 m, we find that C_d ranges from 0.0076 over the flat bottom to 0.0083 over the ridge crest.

Previous experience with ROMS suggests that NPV phenomena such as forced symmetric instability (Wenegrat et al., 2018) are captured to some degree even in moderately coarse hydrostatic simulations (500 m in Wenegrat et al. (2018)). In all our simulations we employ a grid spacing of 300 m in the horizontal and 110 $\sigma-$ levels, to resolve submesoscale and BBL processes. With vertical grid stretching the near bottom vertical resolution is as fine as 0.9 m over the ridge crest and 1.1 m over the flat bottom. Vertical mixing in the BBL is parameterized using KPP (Large et al., 1994; McWilliams et al., 2009). The model also implicitly contains horizontal hyperviscosity and hyperdiffusivity via the third-order upwind-biased scheme (Shchepetkin & McWilliams, 2003, 2005). All the simulations are run for a total of 4 months and time-averages, where shown, are obtained by averaging the relevant quantities over 50 inertial periods. We remark that these time averages are insensitive to the time window during which the averaging is performed provided we exclude the first couple of ridge excursion periods σ_y/V_0, which for the values of σ_y and V_0 chosen in this study, is approximately 16 inertial periods. The displayed averages here are computed over the last 50 intertial periods of the 4 month simulations.

3 Review of 1D and 2D model predictions

In the northern hemisphere, the Ekman transport in a bottom Ekman layer is to the left of the interior geostrophic current. On a slope where the current is prograde, i.e. in the direction of a coastal Kelvin wave, the cross-slope transport results in downwelling of lighter water underneath heavier water, leading to a statically unstable state. Convective mixing then produces a mixed layer which continues to expand in thickness with time (Trowbridge & Lentz, 1991; MacCready & Rhines, 1991). As the BBL thickens, the opposing velocity near the bottom becomes stronger due to thermal wind shear, and the bottom stress weakens. In classical 1D models of slope currents, the BBL continues to deepen until complete Ekman arrest occurs (Garrett et al., 1993). In an upwelling Ekman layer, thermal wind shear similarly acts to reduce the bottom stress. The main difference with respect to the downwelling side is that the upslope advection of buoyancy makes the BBL increasingly stable, and as a result, thinner than on a flat bottom. All the theoretical predictions reviewed in this section assume a constant value of the slope so that $\hat{h}$ below connotes a slope Burger number.

Assuming that in the steady state, the BBL is perfectly well-mixed, Trowbridge and Lentz (1991) derive an estimate for its thickness

$$H_a^{DW} = \frac{V_0}{N\hat{h}}, \tag{9}$$

where the superscript denotes 'downwelling '. However the same authors note that the BBL formed through convective mixing of a downwelling Ekman flow typically tends to be weakly stratified rather than perfectly well-mixed. Brink and Lentz (2010a) derive an arrest time scale for such a weakly stratified BBL assuming a constant gradient Richardson number,

$$T_a^{DW} = \frac{{V_0}^2(1+\hat{h}^2)\Pi(\hat{h})}{2{u_0^*}^2 N\hat{h}^3}, \tag{10}$$

where ${u_0^*}^2$ is the flat-bottom stress in the absence of buoyancy arrest,

$$\Pi(\hat{h}) = \frac{1+\sqrt{1+4Ri_c\hat{h}^2}}{2}, \tag{11}$$

and Ri_c is the critical gradient Richardson number, averaged over an inertial period.

2D simulations (Wenegrat & Thomas, 2020) show that the destruction of the BBL stratification through convective mixing is accompanied by a negative flux of potential vorticity (PV) through the bottom which drives the PV below 0 in the BBL. Here the PV is defined as

$$q = \boldsymbol{\Omega}_a \cdot \boldsymbol{\nabla} b \tag{12}$$

where $b = -g\rho/\rho_0$ is the buoyancy and $\boldsymbol{\Omega}_a = f\hat{\boldsymbol{z}} + \boldsymbol{\nabla}\times\boldsymbol{u}$ is the three-dimensional absolute vorticity, $\hat{\boldsymbol{z}}$ being the unit vector in the z direction.

The $q<0$ state is susceptible to NPV instability modes, which then return the flow to marginal stability. Wenegrat and Thomas (2020) further demonstrate that the onset of instability delays, but does not stop the progression to an arrested state. Their modified arrest time scale is given by

$$T_a^{NPV} = \frac{{V_0}^2(1+\hat{h}^2)^2}{2{u_0^*}^2 N\hat{h}^3}. \tag{13}$$

The extra factor $(1+\hat{h}^2)$ in Eq. (13) comes from substituting $Ri_c = 1+\hat{h}^2$ in Eq. (11), which is the condition of marginal stability with $q=0$ (Allen & Newberger, 1996) . The corresponding expression for the arrest height is

$$H_a^{NPV} = \frac{V_0(1+\hat{h}^2)}{N\hat{h}}. \tag{14}$$

Thus both the arrest time and arrest height are amplified by a factor of $(1+\hat{h}^2)$ relative to 1D models in which NPV instabilities are absent. Note that the modification in the arrest height prediction follows directly from the requirement that $q=0$ in the BBL.

In the upwelling regime, the upslope advection of dense water tends to stabilize the BBL, making it shallower relative to the downwelling. The numerical experiments of Brink and Lentz (2010a) show two different end states, depending on the value of $\hat{h}$. For $\hat{h} > 1$, their solutions produce a uniformly stratified BBL connecting smoothly to the stratified interior. The BBL height corresponding to arrest is

$$H_a^{UW} = \frac{V_0}{N\hat{h}}\gamma(\hat{h}), \tag{15}$$

where the superscript denotes 'upwelling ' and $\gamma(\hat{h})$ is given by the functional form

$$\gamma(\hat{h}) = \frac{-1+\sqrt{1+4Ri^{UW}\hat{h}^2}}{2}. \tag{16}$$

Brink and Lentz (2010a) further find that $Ri^{UW} = 0.4$ produces a satisfactory fit to their numerical experiments, using either a Mellor-Yamada 2.0 closure or $k-\varepsilon$ model. The corresponding arrest time scale for the upwelling favorable regime is then obtained as

$$T_a^{UW} = \frac{V_0^2(1+\hat{h}^2)\gamma(\hat{h})}{2u_0^{*2}N\hat{h}^3}. \tag{17}$$

On the other hand, when $\hat{h} < 1$, the vertical structure is characterized by a weakly stratified BBL, capped by a strongly stratified pycnocline (Brink & Lentz, 2010a). Buoyancy adjustment times are much longer than for $\hat{h} > 1$. In the limit $\hat{h} \ll 1$, the BBL characteristics approach those of a flat bottom Ekman layer. Interestingly, in their recent LES study, Ruan, Thompson, and Taylor (2021) note that capped BBLs are not observed. The authors attribute this to relaminarization of the BBL, which does not occur in simpler turbulence closures. For more details on the capped BBL we refer the reader to Brink and Lentz (2010a).

In one and two dimensional models of slope currents, buoyancy adjustment is a defining aspect of the solutions in both the $\hat{h} > 1$ and $\hat{h} < 1$ regimes. The only difference is the considerably longer adjustment time when $\hat{h} < 1$. This can be seen by inspecting Eqs. (10) and (13) where in the limit $\hat{h} \ll 1$, T_a^{NPV} varies as $\hat{h}^3$ and T_a^{UW} as $1/\hat{h}$. By contrast, in the case of an isolated 3D ridge, the $\hat{h} \ll 1$ regime is quasi-geostrophic (QG) (Schär & Davies, 1988), with strong cross-isobath flow and vortex stretching/squeezing dominating the dynamics (Hogg, 1973). This regime is more or less fully described by the QG potential vorticity conservation equation (Schär & Davies, 1988). We note that the parameter space $\hat{h} < 1$ was also revisited recently by Srinivasan et al. (2019) using high resolution, BBL-resolving ROMS solutions of flow past a circular seamount. A notable finding of this study was that, even with bottom drag and a resolved BBL, a non-eddying steady QG state is always reached for $\hat{h} < 0.6$. These results are consistent with the earlier theoretical predictions of Hogg (1973) and Schär and Davies (1988) for QG flow over 3D topog-

raphy. The characteristic feature of the QG solution is the emergence of an isolated anticyclone, also known as a Taylor cone (Hogg, 1973) atop the seamount (see also. Fig. 1 of Srinivasan et al., 2019). For the elongated ridge we similarly find that QG dynamics prevails for values of $\hat{h}$ as high as 0.8. For this reason, we do not dwell on the $\hat{h} < 1$ regime in this paper. Instead, concentrating on the $\hat{h} > 1$ regime, we will see that the evolution toward Ekman arrest in a 3D topographic encounter problem has important differences from the lower dimensional temporal spin up problems. In particular, nonlinear straining plays an important role, both in weakening the ageostrophic BBL shear during the initial encounter with the ridge, as well as the subsequent evolution of the BBL towards thermal wind balance.

4 Results

4.1 Bottom Stress Evolution on the Slopes

We define the anticyclonic (cyclonic) side of the ridge as the side where uphill is to the right (left) of the incident flow. Note that, in our flow configuration (Fig. 1) with the Coriolis frequency $f > 0$, the bottom Ekman layer is downwelling-favorable on the anticyclonic side and upwelling-favorable on the cyclonic side. In the discussion that follows, the BBL height on the cyclonic side refers to the region of active turbulence where shear driven entrainment and mixing are occuring. This is also the quantity explicitly computed in ROMS using the KPP formulation (McWilliams et al., 2009).

On the anticyclonic side, a dynamically consistent definition of the BBL height needs to account for convective mixing produced by the downwelling Ekman layer as well as secondary NPV instabilities. Allen and Newberger (1996) show that, in a downwelling Ekman layer, symmetric instability partially restratifies the BBL so that its stratification at marginal stability ($q = 0$) is given by $N^2\hat{h}^2/(1+\hat{h}^2)$. Thus for values of $\hat{h}$ greater than 1, the BBL can retain substantial stratification. This is well supported by recent observations in the Orkney passage (Garabato et al., 2019) where the measured $\hat{h}$ is about 1.8 and the BBL stratification is around two-thirds of the interior value. The solutions analyzed here have $\hat{h}$ values ranging from 1.6 to 12.8 and as we shall see below, are unstable to NPV instabilities on the anticyclonic side.

One choice of definition for the BBL height therefore is as the depth over which the vertical buoyancy gradient is less than $N^2\hat{h}^2/(1+\hat{h}^2)$. However our 3D solutions depart from the 2D assumptions implicit in Allen and Newberger (1996) in some important respects: first, the stratification is not constant in the BBL and so the BBL is never uniformly in a state of marginal

stability; second, as we will see later, the instabilities that develop are not pure symmetric modes but rather hybrid modes that draw energy from both the mean vertical shear *and* horizontal shear. Thus we simply define the BBL height as the height from the bottom where the stratification first exceeds $\alpha N^2\hat{h}^2/(1+\hat{h}^2)$, where α is some constant slightly larger than 1, here taken to be 1.1. A 10% variation in α (say $\alpha = 1.2$ rather than 1.1) does not lead to a material difference in the computed BBL heights.

The incident flow on the flat bottom has a well-mixed, turbulent BBL, capped by a strongly stratified pycnocline. The characterstics of the flat bottom Ekman layer have been previously described by other authors (e.g. Taylor & Sarkar, 2008). Fig. 1a shows the evolution of the bottom stress as this flat bottom Ekman layer encounters the topography. The stress values have been normalized by $\rho_0 C_d^* V_0^2$, the expected stress on a flat bottom with far-field velocity V_0. The value of the drag coefficient C_d^* when this formula is used, is typically in the range 0.002-0.003 (Sen et al., 2008; Arbic et al., 2009). Note that C_d^* is different from C_d used to parameterize the bottom stress in ROMS because the latter is multiplied by V_b^2 (V_b is the velocity in the bottom-most σ-layer) and not V_0^2 to get the bottom stress (see Eq. 8). Here we find that $C_d^* = 0.0022$ yields a non-dimensional stress around 1 away from the topography and use this value henceforth in our scalings for stress, energy production and dissipation.

The sustained weakening of the stress on the slopes is apparent in Fig. 1a. To better visualize its downstream evolution in a slope-averaged sense, we compute the average stress across the set of barotropic streamlines depicted in this figure, separately on each side of the ridge, and plot this as a function of along-streamline distance (Figs. 3a,b). The bottom stress starts to decrease within a short distance of the well-mixed BBL encountering the ridge. The reduction is stronger for larger $\hat{h}$, approaching more than an order of magnitude for $\hat{h} = 3.2$ and higher (Fig. 3).

On the anticyclonic (downwelling) side, the mean streamlines in Fig. 1a show that the current remains largely attached to the slopes throughout the encounter. As a result, along-stream fluctuations are muted. By contrast, there are large oscillations on the cyclonic side associated with the separation and reattachment of eddies during the early encounter (visible in Fig. 1b).

After the early rapid reduction, the boundary stress exhibits a relatively slow increasing tendency downstream. This can be understood as follows. In response to the diminishing bottom

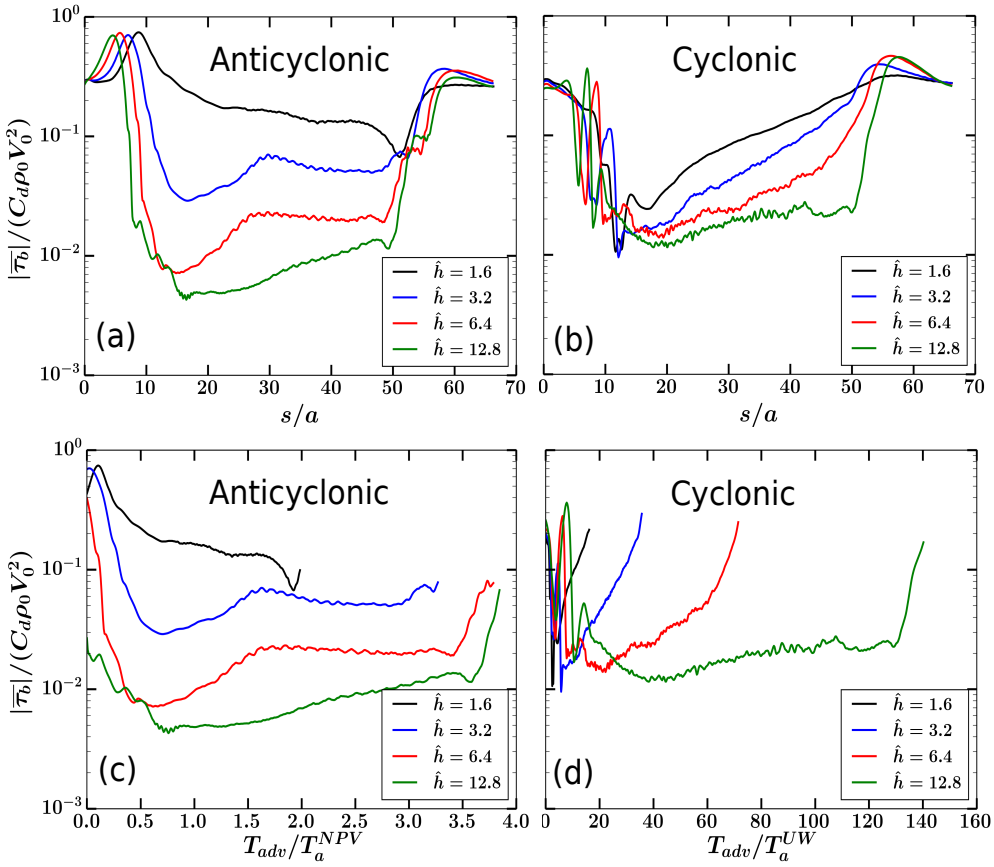

Figure 3. (Top panel) Streamline-averaged evolution of the time-averaged bottom stress shown in Fig. 1 for different values of $\hat{h}$. (a) Anticyclonic and (b) Cyclonic. (Bottom panel) Evolution of the bottom stress as a function of time. Here $T_{adv} = (s - s_0)/V_0$, where s is the distance travelled along the mean streamline starting from the inflow location $y = 0$, and s_0 is the value of s where the streamline intersects the ridge contour $h(x,y) = h_m \exp(-2)$. Thus T_{adv} is an advective time representative of the transit time of the flow along the ridge slopes. (c) Anticyclonic and (d) Cyclonic. T_a^{NPV} is the time scale for arrest in the presence of NPV instabilities, as derived in Wenegrat and Thomas (2020) (Eq. (13) above) and T_a^{UW} is the Brink and Lentz (2010a) time scale for arrest in the upwelling-favorable regime (Eq. (17) above).

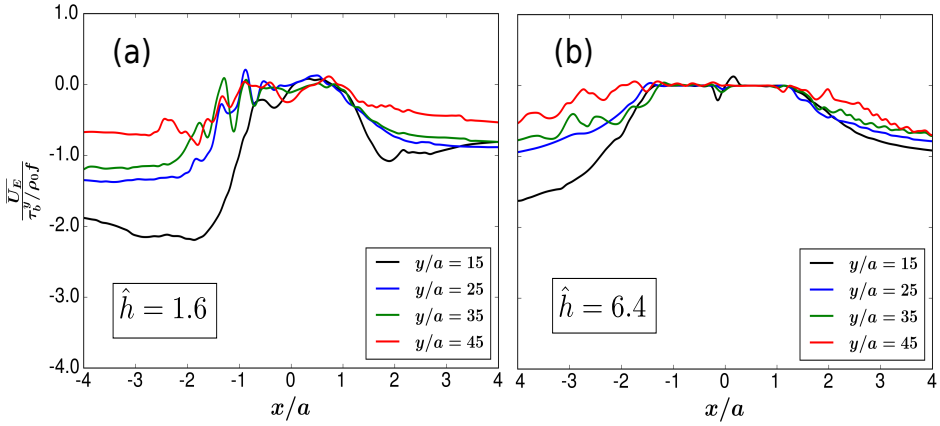

Figure 4. Downstream evolution of the Ekman transport (defined in Eq. (18)) at different downstream locations given by the non-dimensional distance y/a, on and immediately adjacent to the ridge slopes. The values have been normalized by the average Ekman transport over the flat bottom far from the ridge. The $\hat{h}$ values are indicated inside each panel.

stress, the cross-slope BBL Ekman transport

$$U_E = \int_{-H}^{-H+h_{bbl}} u \, \mathrm{d}z \tag{18}$$

at the upper slopes $|x/a| < 0.5$, approaches zero within a short distance downstream on both sides of the ridge (Fig. 4). The resulting zonal divergence in Ekman transport drives a secondary circulation in the vertical plane (Fig. 5). This circulation, which has a upwelling/downwelling tendency on the cyclonic/anticyclonic side respectively will tend to accelerate the along-slope flow. Feedback of the secondary circulation into the interior along-slope flow was also reported by Benthuysen et al. (2015) in their 2D simulations of flow past a shelf break. Note that in their case, the feedback was purely temporal (as the simulations were 2D); here however, the secondary circulation will tend to induce a more complicated spatio-temporal feedback into the interior flow. On the cyclonic side, the upwelling BBL causes the isopycnals to squeeze together during the downstream adjustment (as seen, for e.g. in Fig. 2 of Jagannathan et al., 2021), which also has an accelerating effect on the along-slope flow.

We plot the quasi-temporal evolution of the stress along the barotropic streamlines by defining an advective time

$$T_{adv} = \frac{s - s_0}{V_0}. \tag{19}$$

Here s is the along-streamline distance measured from the inflow location $y = 0$, averaged across the barotropic streamlines shown in Fig. 1. Note that the averaging is performed separately on

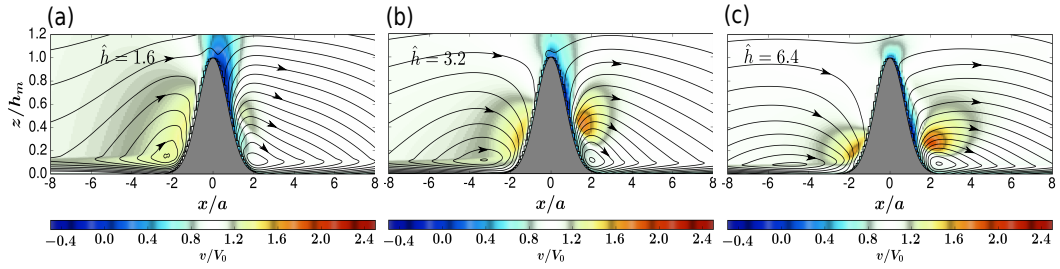

Figure 5. Time mean streamlines in the vertical plane of the flow-field obtained by averaging u and w over the straight section of the ridge $15 \leq y/a \leq 45$. Also displayed are contours of the normalized along-slope velocity v/V_0. $\hat{h}$ values are indicated inside each panel. Note that, as the real flow-field is three-dimensional, these streamlines are not true pathlines of the flow, rather they represent a 2D projection that gives a qualitative view of the secondary circulation above the ridge slopes.

each side of the ridge. s_0 is the value of s where the streamline intersects the ridge contour $h(x,y) = h_m \exp(-2)$. That is, the clock starts ticking where the mean streamline encounters the ridge and T_{adv} represents the transit time of the flow on the slopes. We use T_a^{NPV} and T_a^{UW} respectively to scale the advective time T_{adv} on the anticyclonic and cyclonic sides. Note that for all the values of $\hat{h}$ considered here, T_a^{NPV} is significantly longer than T_a^{UW}. Figs. 3c,d show that the bottom stress slumps by an order of magnitude over $\mathscr{O}(1)$ arrest time scale (T_a^{NPV}) on the anticyclonic side and between $\mathscr{O}(1) - \mathscr{O}(10)$ arrest time scales on the cyclonic side. Plugging in $V_0 = 0.105\,\mathrm{ms}^{-1}$, $u_0^{*2} = C_d^* V_0^2$, with $C_d^* = 0.0022$ (Sen et al., 2008; Arbic et al., 2009), and N and $\hat{h}$ for each solution in Eqs. (13) and (17), we find that this corresponds to $\mathscr{O}(1)$ inertial periods on each side. As we shall show in section 4.2 in our analysis of the vertical shear equation Eq. (21), this initial rapid stress reduction is not due to buoyancy adjustment, but rather a consequence of 3D, nonlinear straining effects when the flow first encounters the ridge.

The flow on the anticyclonic side develops a spatial instability mode which grows to finite amplitude downstream. This is manifested by the emergence of a banded pattern of small scale vortices in Fig. 1b. The instability begins further and further upstream for increasing values of $\hat{h}$. Below we will identify these as belonging to a general class of NPV instabilities. In the 2D simulations of Wenegrat and Thomas (2020), the flow continues to evolve toward an arrested state even after the onset of NPV instabilities. From Eq. (13), we would expect that this 2D arrest time scale T_a^{NPV} is approximately 7.8 inertial periods for the case $\hat{h} = 1.6$ and 4.3 inertial periods for $\hat{h} = 12.8$. The encounter time in our solutions is around 16 inertial periods on the anticyclonic side (Fig. 3c,d). Thus the 2D expectation of buoyancy adjustment (e.g. Fig. 16 of Wenegrat and

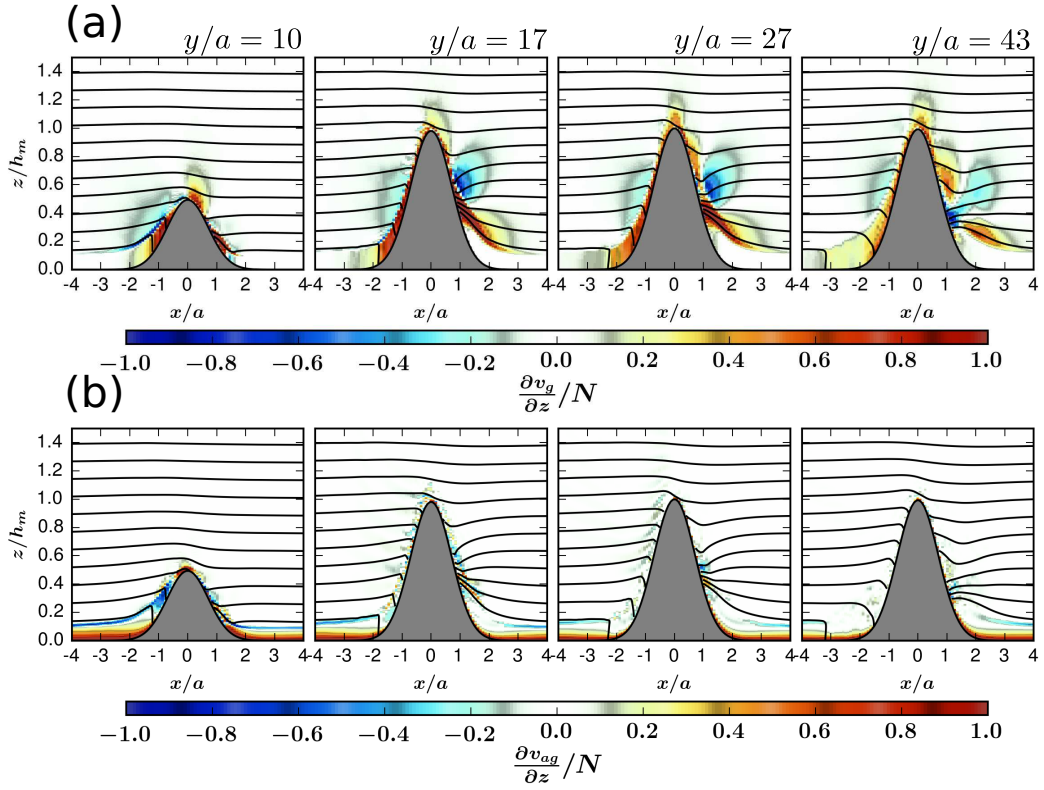

Figure 6. Downstream evolution of the time-averaged y component of the vertical shear overlain with the flow isopycnals (a) geostrophic vertical shear $\frac{\partial v_g}{\partial z}/N$ and (b) the ageostrophic shear $\frac{\partial v_{ag}}{\partial z}/N$ for the $\hat{h} = 3.2$ solution. The ridge centerline is at $y/a = 30.9$.

Thomas (2020)) is a monotonic decay of the bottom stress toward zero before the flow separates from the ridge. Yet in Fig. 3, the bottom stress exhibits a much slower decay than expected for $\hat{h} = 1.6$. For the two intermediate values of $\hat{h}$, there is a slight increase after the initial slump, followed by a plateauing of the stress. Likewise, the bottom stress on the cyclonic side plunges sharply during the initial encounter but starts to rebound to higher values over $\mathcal{O}(10)$ arrest time scales. The observations above are indicative of the fact that other 3D effects besides buoyancy adjustment exert a strong influence on bottom stress evolution, and hence turbulent bottom dissipation over topographic ridges. We will examinine these in detail below.

4.2 Vertical Shear Balance and the Role of Strain

The theoretical state of Ekman arrest is characterized by collapse of the BBL on the slopes and the establishment of a deep boundary layer in a state of thermal wind balance. To assess the degree of arrest in our solutions, we decompose the time-averaged vertical shear $\boldsymbol{u}_z$ into its geostrophic

and ageostrophic components,

$$\frac{\partial \boldsymbol{u}_g}{\partial z} = \frac{1}{\rho_0}\hat{\boldsymbol{z}} \times \boldsymbol{\nabla}_H b, \tag{20a}$$

$$\frac{\partial \boldsymbol{u}_{ag}}{\partial z} = \frac{\partial \boldsymbol{u}_H}{\partial z} - \frac{\partial \boldsymbol{u}_g}{\partial z}, \tag{20b}$$

where it is recalled $b = -g\rho/\rho_0$ is the buoyancy, $\boldsymbol{\nabla}_H b$ is its horizontal gradient and $\boldsymbol{u}_H$ is the horizontal velocity vector. Note that the ageostrophic component here encompasses not only shear due to vertical mixing in the BBL but also that due to nonlinear advective effects such as strain (see Eq. (21) below).

In all our solutions, the along-slope component of the vertical shear $\partial v/\partial z$ is much larger than its cross-slope counterpart $\partial u/\partial z$. As such the along-slope component of vertical shear is also the quantity of interest in the downstream buoyancy adjustment problem. Fig. 6 is a representative plot of the time-averaged, vertical shear decomposition for the case $\hat{h} = 3.2$. Over the flat bottom ($|x/a| > 3$) the shear in the BBL is purely ageostrophic and is positive except near the pycnocline (see also Taylor & Sarkar, 2008). Shortly after the current-ridge encounter, at $y/a = 10$, both the geostrophic and ageostrophic components are significant. Furthermore, on the anticyclonic side, the two components are clearly seen to be opposite-signed, with the ageostrophic shear being negative. At $y/a = 17$ the geostrophic component is clearly dominant while the ageostrophic component has weakened drastically (Fig. 6). It continues to further weaken downstream, signalling approach toward a partially arrested state. Interestingly, the rightmost panel of this figure shows that the geostrophic shear itself has relatively weakened by $y/a = 43$. As we shall see in section 4.3 this reflects partial restratification of the BBL following the onset and growth of NPV instabilities.

Writing the squared vertical shear as $||\boldsymbol{u}_z||^2 = u_z^2 + v_z^2$, its Lagrangian evolution equation can be written as (Srinivasan et al., 2021)

$$\frac{1}{2}\frac{D||\boldsymbol{u}_z||^2}{Dt} = \underbrace{-\left[\underbrace{(u_z^2 u_x + v_z^2 v_y) + u_z v_z (u_y + v_x)}_{-\Lambda_h} + \underbrace{||\boldsymbol{u}_z||^2 w_z}_{-\Lambda_v}\right]}_{\Lambda_{nl}} \underbrace{-(b_x u_z + b_y v_z)}_{\Lambda_b} + \underbrace{D(\boldsymbol{u}_z)}_{\Lambda_{mix}}, \tag{21}$$

where $\Lambda_{nl} = \Lambda_h + \Lambda_v$ represents nonlinear horizontal and vertical straining effects, Λ_{mix} is the shear generation/destruction due to the combined effect of parameterized vertical momentum mixing and implicit horizontal hyperdiffusion, and Λ_b is the geostrophic production term. We plot the time-average of each of the tendency terms on the RHS of Eq. (21) for the three solutions $\hat{h} =$ 1.6, 3.2 and 6.4 in Fig. 7. The terms are averaged across-slope and over the local BBL depth on the anticyclonic side. We do not show an equivalent plot for the cyclonic side as the flow there

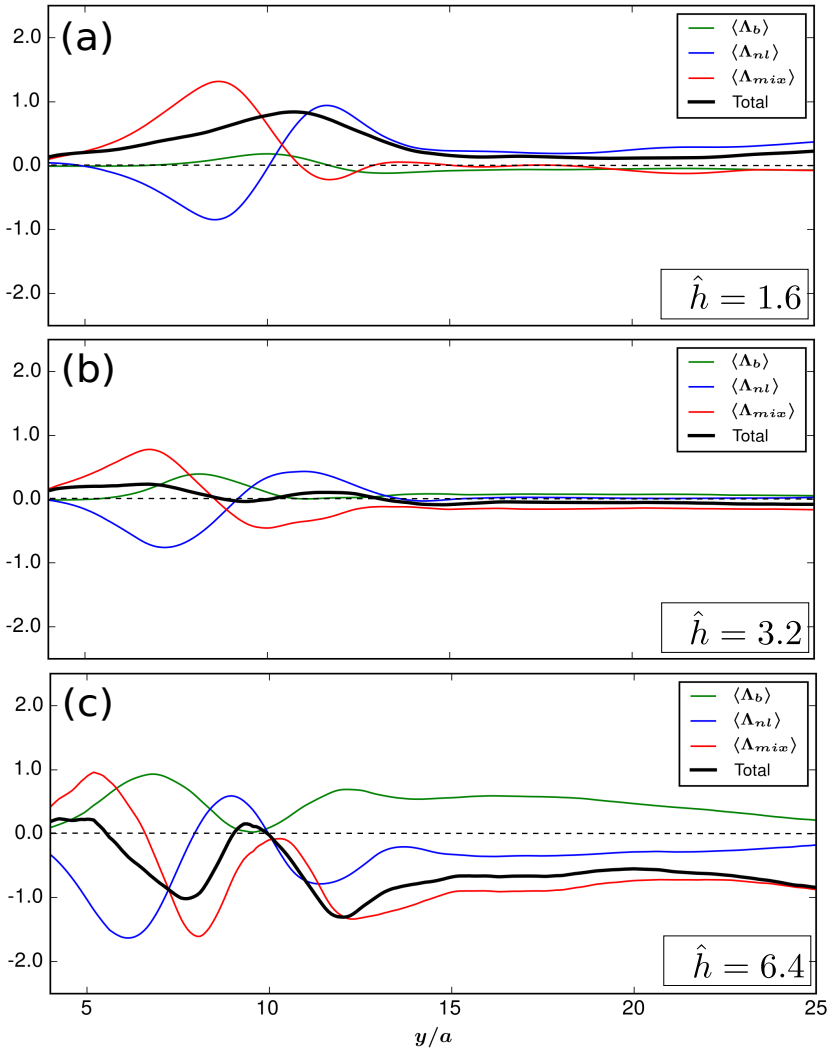

Figure 7. (Anticyclonic) Tendency terms of the time-averaged squared vertical shear equation Eq. (21) for (a) $\hat{h} = 1.6$, (b) $\hat{h} = 3.2$ and (c) $\hat{h} = 6.4$. Λ_{nl} represents nonlinear straining effects, Λ_{mix} is the shear generation/destruction due to the combined effect of parameterized vertical momentum mixing and implicit horizontal hyperdiffusion in ROMS, and Λ_b is the geostrophic production term. Each term is normalized by $NV_0^2 h_m^{-2}$ and averaged over the local BBL depth and in the across-slope direction. $\hat{h}$ values are indicated inside each panel. The zero line is shown dashed for clarity.

separates early, and consequently there is no obvious trend to be discerned from examining Eq. (21).

Eq. (21) by construction, obscures information regarding the sign of the vertical shear; its virtue is that it is in the form of a Lagrangian evolution equation of a positive definite quantity $||\boldsymbol{u}_z||^2$ whose tendency terms are conveniently partitioned into those associated with mixing, buoyancy or nonlinear straining processes (note that the Coriolis term drops out). Useful insight can thus be gained by tracking the downstream evolution of these terms alongside a visual inspection of the vertical shear decomposition itself. Compared to the depth integrated vertical shear which can have significant cancellations when both positive and negative shear regions are present (e.g. Fig. 6), the sign definiteness of $||\boldsymbol{u}_z||^2$ makes its depth integrated evolution relatively straightforward to interpret. Before the flow encounters the ridge, turbulent vertical mixing is the primary source of vertical shear generation in the BBL. This ageostrophic shear is neutralized by nonlinear straining processes during the early flow adjustment over the topography. Examining Fig. 6 alongside Fig. 7b one can infer that the negative ageostrophic shear over the anticyclonic slopes at $y/a = 10$ comes largely from nonlinear straining effects Λ_{nl}. Buoyancy adjustment and strain then combine to bring the flow downstream progressively closer to a state of geostrophic balance. Downstream of $y/a \approx 12$, note that the total tendency remains slightly negative. This is consistent with the observed reduction in the intensity of the geostrophic vertical shear at $y/a = 43$ (rightmost panel of Fig. 6).

Note that the peaks and troughs of all the tendency terms shift upstream with increasing $\hat{h}$, reflecting faster adjustment times for higher $\hat{h}$ (Eqs. (10), (13)). A comment on Fig. 7c which shows the tendency terms for $\hat{h} = 6.4$: interestingly, the combined effect of Λ_{nl} and Λ_{mix} produces two prominent troughs in the total squared vertical shear tendency. The exact reason for this pattern is not clear; however the relatively large negative value of the total tendency downstream of $y/a = 15$ is consistent with the expected strong restratifying effects in the BBL for high $\hat{h}$ (Allen & Newberger, 1996) which will tend to substantially weaken the geostrophic vertical shear.

Strong nonlinear, 3D straining motions during the initial flow adjustment over the ridge thus strongly influence the dynamics of buoyancy adjustment on the slopes. In particular, the strain term neutralizes the ageostrophic BBL shear of the incident flow, and then acts in concert with the geostrophic production term Λ_b to produce a more rapid initial stress reduction (Fig. 3c,d) than predicted by 1D or 2D models where strain effects are absent. Note that this is a rather dif-

ferent phenomenological sequence compared to 1D models where buoyancy adjustment alone acts to convert ageostrophic shear to geostrophic shear.

4.3 BBL instabilities, energetics and dissipation

The conversion from ageostrophic to geostrophic vertical shear in the BBL is associated with an expanding region of negative PV. Figs. 8a,b show the evolution of the stratification and PV over the anticyclonic slope for the $\hat{h} = 3.2$ solution. A well-mixed BBL with potential vorticity $q \approx 0$ encounters the topography. The BBL is capped by a thin, strongly stratified pycnocline (c.f. Taylor & Sarkar, 2008) where both the stratification and PV are posiive. The lower part of the BBL initially develops NPV due to convective overturning (Fig. 8b). The region of weak stratification deepens and the pycnocline is also eventually destroyed further downstream (Fig. 8a). As the geostrophic vertical shear is established, the NPV layer becomes increasingly deeper.

The $q < 0$ state is susceptible to instability, which can be categorized in different ways depending on the the dominant energy conversion terms (Wang et al., 2014; Thomas et al., 2013). Fig. 8c shows that the horizontal component $q_h \approx -v_z b_x$ partially contributes to the negative PV in the mixed layer, hinting at the possibility of symmetric instability (Thomas et al., 2013). To gain further insight into the nature of the instability here (visible as bands of instability on the anticyclonic side in the bottom row of Fig. 1), we compute the production terms of the eddy kinetic energy (EKE) equation. Energy is transferred from the mean flow to the eddies through the vertical and horizontal Reynolds stress work, defined respectively as

$$VRS = -(\overline{u'w'}\,\overline{u}_z + \overline{v'w'}\,\overline{v}_z), \tag{22}$$

and

$$HRS = -(\overline{u'u'}\,\overline{u}_x + \overline{u'v'}\,\overline{u}_y + \overline{v'v'}\,\overline{v}_y + \overline{u'v'}\,\overline{v}_x), \tag{23}$$

where the overbar $\overline{(\cdot)}$ denotes a time average and primed quantities $(\cdot)'$ are preturbations about the average. Reversible exchange of available potential energy (APE) between the mean and eddy fields also occurs through the vertical buoyancy flux

$$VBF = \overline{w'b'}. \tag{24}$$

All the production terms are normalized by $C_d^* V_0^3$, a commonly used scaling (Sen et al., 2008; Arbic et al., 2009; Ruan, Wenegrat, & Gula, 2021) for energy dissipation within a flat bottom turbulent BBL with bottom stress $\rho_0 C_d^* V_0^2$, where C_d^* is again taken to be 0.0022. Fig. 9 shows that

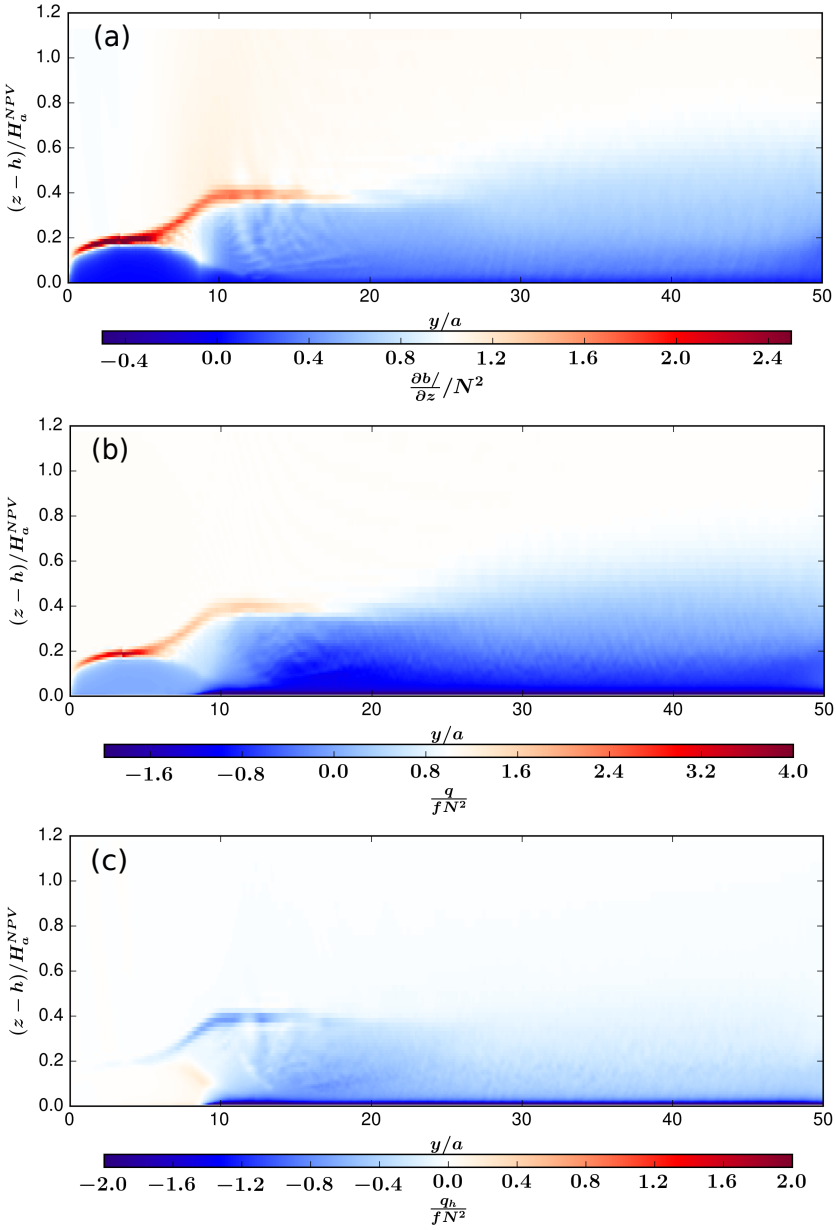

Figure 8. Downstream evolution of the time-averaged vertical buoyancy gradient and PV on the anticyclonic side for the $\hat{h} = 3.2$ solution. Over the ridge, each of the quantities is averaged across the slope and plotted as a function of height from the ridge bottom, normalized by H_a^{NPV}, the predicted value of NPV instability-modulated arrest height in Wenegrat and Thomas (2020) (Eq. (14)). On the flat bottom before the encounter, the color contours displayed are for the centerline $x/a = 0$ values. (a) $\partial b/\partial z$ normalized by the background squared Brunt Vaisala frequency N^2. (b) Normalized potential vorticity q/fN^2 and (c) the horizontal component of potential vorticity q_h/fN^2.

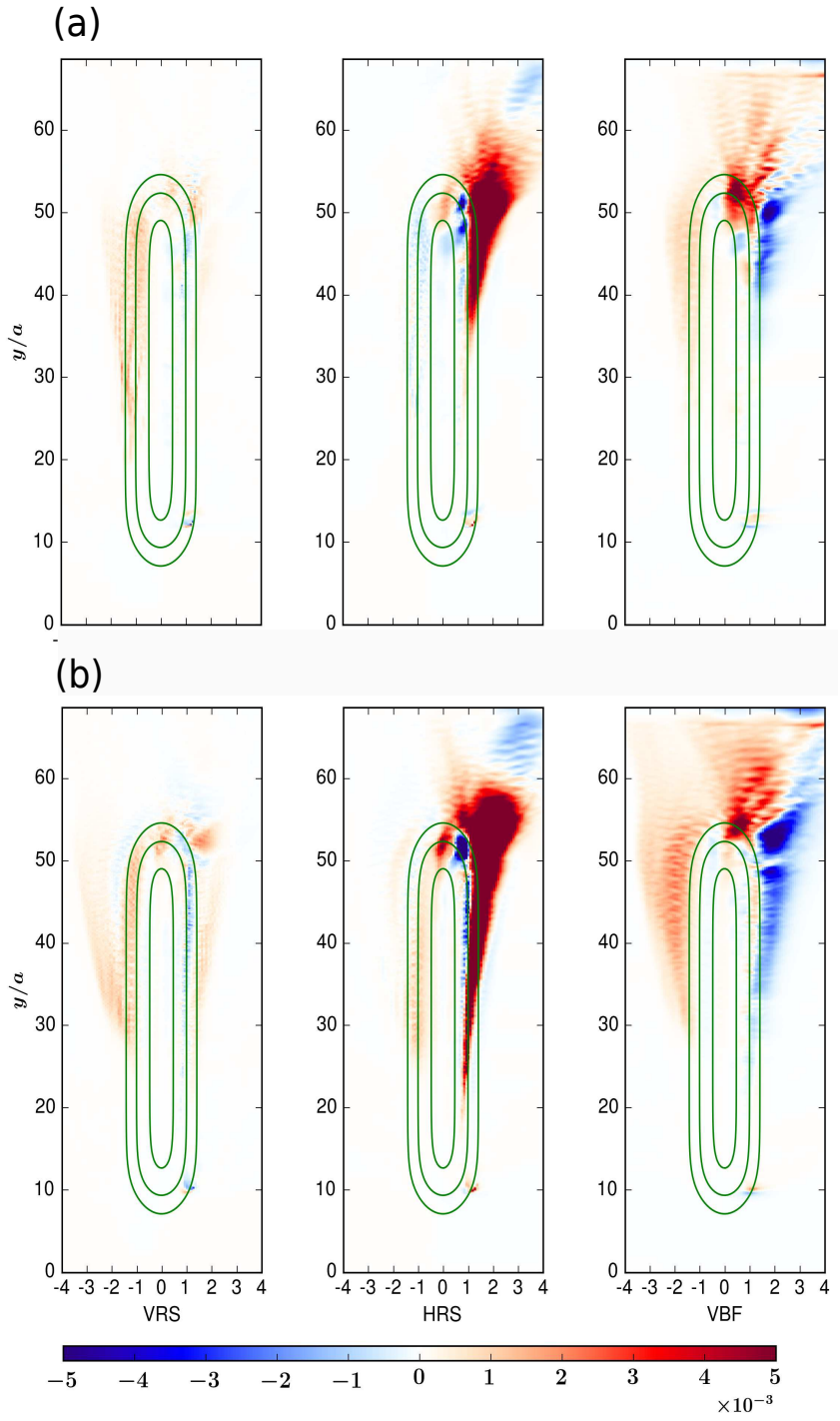

Figure 9. Time-averaged, vertically integrated EKE production terms (Eqs. (22), (23) and (24) for (a) $\hat{h} = 1.6$ and (b) $\hat{h} = 3.2$. A Gaussian filter has been applied to VBF to remove grid scale noise downstream of the ridge. All quantities are non-dimensionalized by $C_d^* V_0^3$, with $C_d^* = 0.0022$, and the colomap is saturated at 6×10^{-1}.

conversion of energy from the mean flow to the eddies on the anticyclonic side is accomplished primarily by VRS and VBF at $\hat{h} = 1.6$, and through a combination of VRS, HRS and VBF at $\hat{h} = 3.2$. In the dynamical framework of Thomas et al. (2013) and Wenegrat and Thomas (2020), the former may be classified as a hybrid symmetric/gravitational instability and the latter a hybrid symmetric/centrifugal/gravitational instability. The instability tends to restratify the BBL, bringing the flow back toward a state of marginal stability $q \approx 0$ (Fig. 8b,c). VBF is primarily responsible for the restratification, converting available potential energy to EKE in the process. Note that the large VBF contribution well downstream of the ridge centerline may also indicate the presence of a hybrid baroclinic mode on the anticyclonic side. The restratification in the BBL and the corresponding reduction in the geostrophic vertical shear can be seen in the rightmost panel of Fig. 6a ($y/a = 43$). For the larger $\hat{h}$ cases, partial restratification of the BBL following the onset NPV instabilities manifests as a net sink in the Lagrangian vertical shear equation (black line in Fig. 7c).

On the cyclonic side, EKE production is overwhelmingly from HRS, and is substantially more intense compared to the anticyclonic side. This is strongly indicative of a horizontal, inflectional point instability of the mean flow, similar to that seen, for example, in submesoscale and BBL resolving simulations of topographic wakes in the Southwestern Pacific (Srinivasan et al., 2017). VBF, which acts as minor sink of EKE, represents conversion from EKE to available potential energy resulting from the upslope advection of buoyancy. Fig. 9 also shows that HRS conversion commences further upstream for the $\hat{h} = 3.2$ case compared to $\hat{h} = 1.6$. The onset of horizontal barotropic instability on the topographic slopes could partly explain why the strip of cyclonic vorticity generated through the Bottom Stress Divergence Torque (Jagannathan et al., 2021) detaches from the slopes further upstream compared to the anticyclonic side. As seen in Fig. 3b,d, for all $\hat{h}$ considered, the early separation reverses the decaying trend of bottom stress on the cyclonic side, past $s/a \approx 20$ (where s is the along-streamline distance).

Note that in Fig. 9, VBF is qualitatively higher for $\hat{h} = 3.2$ when compared to $\hat{h} = 1.6$. However, Perfect et al. (2020a) found a decrease in the VBF term with increasing Burger number (equivalently $\hat{h}$ here) for their axisymmetric Gaussian ridge solutions. We hypothesize that this discrepancy is atleast partially attributable to the geometry of the ridge considered here. The sloping BBL on the elongated ridge is likely more prone to buoyancy adjustment dynamics compared to the seamount solutions of Perfect et al. (2020a). This affects the VBF term in the following ways - VBF is active during both the initial convective instability in the downwelling BBL on the anticyclonic side as well as the later restratification of the BBL, creating EKE at the ex-

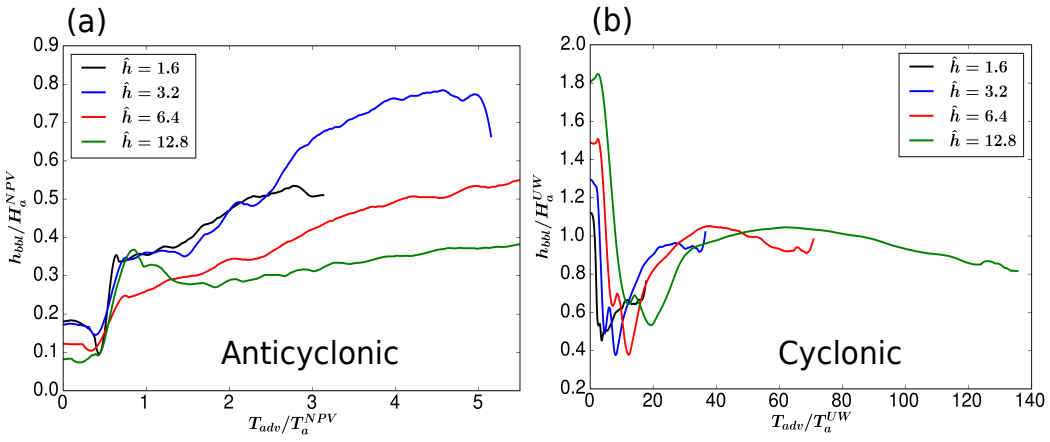

Figure 10. (a) Evolution of the cross-slope averaged BBL depth h_{bbl} as a function of the advective time T_{adv}. Recall that $T_{adv} = (s - s_0)/V_0$ is the along-streamline distance expressed as a time scale. (a) On the anticyclonic side, normalized by the Wenegrat and Thomas (2020) prediction for the arrest height (Eq. (14)) when NPV instabilities are active. (b) On the cyclonic side, normalized by the Brink and Lentz (2010a) prediction (Eq. (15)) for an upwelling Ekman layer

pense of APE. Likewise upslope buoyancy advection on the cyclonic side converts EKE to APE (and thus is a sink of APE). The magnitude of both these EKE $\longleftrightarrow$ APE conversions increases with N and thus with $\hat{h}$ (which is varied in our simulations by changing N). We refer the reader to Umlauf et al. (2015) for further discusson of the energetics of BBL buoyancy adjustment.

As in the case of observations by Garabato et al. (2019) and solutions of Wenegrat and Thomas (2020), the BBL on the downwelling (anticyclonic) side remains substantially stratified in our solutions (Fig. 8a). Recall the definition of the BBL on the downwelling side as the height from the bottom where the stratification first exceeds $1.1N^2\hat{h}^2/(1+\hat{h}^2)$ (see section 4.1). In Fig. 10a we show the downstream evolution of the across-slope averaged BBL thickness h_{bbl} on the anticyclonic side. The values are non-dimensionalized using the predicted value of NPV instability-modulated arrest height in Wenegrat and Thomas (2020) (Eq. (14)). The BBL deepens downstream as the flow evolves along the slopes, but in all cases, its depth is less than the predicted value when the current separates off the slopes. On the cyclonic side, the stabilizing effect of upslope buoyancy advection is expected to shrink the boundary layer thickness, relative to the upstream flat-bottom value (Brink & Lentz, 2010a). Fig. 10b shows that h_{bbl} decreases sharply during the initial encounter, even beyond the value predicted in Brink and Lentz (2010a). Further downstream, h_{bbl} slowly approaches H_a^{UW}. However, as noted earlier, the separation of the cur-

rent from the slopes and the slow increase observed in the bottom stress (Fig. 3b,d) are indicative of the BBL not being fully arrested.

The loss of energy due to dissipation can be partitioned into that from the mean kinetic energy (MKE) of the parameterized BBL turbulence, $\bar{\varepsilon}$, and that due to the forward cascade initiated by the ageostrophic instabilities, ε'. Recall that eddy dissipation in ROMS occurs through both the parameterized vertical Reynolds stress $\boldsymbol{\tau}_z$ as well as a horizontal hyperdiffusion term that is implicit in the third order upwind biased scheme for computing horizontal advection. To quantify the influence of the topography on dissipation, $\bar{\varepsilon}$ and ε' are defined here as area averages over the sloping sides of the ridge. For example on the anticyclonic side,

$$\bar{\varepsilon} = \frac{\iint_A \int_{-H}^{-H+h_{bbl}} \bar{\boldsymbol{u}} \cdot \left(\overline{\boldsymbol{\tau}_z} + \overline{\mathscr{D}_H \boldsymbol{u}}\right) \mathrm{d}z\,\mathrm{d}y\,\mathrm{d}x}{\iint_A \mathrm{d}y\,\mathrm{d}x} \tag{25a}$$

$$\varepsilon' = \frac{\int_{-\infty}^{0}\int_{-\infty}^{\infty}\int_{-H}^{\eta} \overline{\boldsymbol{u}' \cdot \left(\boldsymbol{\tau}_z' + \mathscr{D}_H \boldsymbol{u}'\right)}\,\mathrm{d}z\,\mathrm{d}y\,\mathrm{d}x}{\iint_A \mathrm{d}y\,\mathrm{d}x}, \tag{25b}$$

where η is the sea surface elevation, $\mathscr{D}_H$ denotes the horizontal hyperdiffusion term on the RHS of the horizontal momentum equations. A is the region bounded by the y-axis and some low-level bathymetric contour, here taken to be the contour on which the ridge height decays to $\exp(-2)$ of its maximum value h_m,

$$A = \{x, y \,|\, x \leq 0; h(x,y) > h_m \exp(-2)\}, \tag{26}$$

The dissipation fractions $\bar{\varepsilon}$ and ε' and slope region A are defined analogously for the cyclonic side.

Eq. (25a) represents the area-averaged MKE dissipation from the BBL over the sloping sides of the ridge. The 'slope effect 'on BBL dissipation is visible when we plot $\bar{\varepsilon}$ normalized by $C_d^* V_0^3$ (Fig. 11a) for each $\hat{h}$ solution. For $\hat{h} = 1.6$, the dissipation rate of MKE on the anticyclonic side is around 75% of that expected from the flat-bottom scaling $C_d^* V_0^3$, reflective of moderate bottom stress reduction. As $\hat{h}$ increases, the normalized $\bar{\varepsilon}$ decreases, falling to as low as 0.1 for $\hat{h} = 12.8$. The diminished $\bar{\varepsilon}$ is indicative of partial arrest of the BBL.

The numerator of Eq. (25b) is the volume integral of the EKE dissipation over the total fluid volume on the anticyclonic side and not just within the BBL as is the case in Eq. (25a). This choice reflects the fact that the instabilities spawned on the slopes give rise to eddies which generally dissipate over a broad wake region rather than locally (c.f. Srinivasan et al., 2021). Dividing the total eddy-induced dissipation by $\iint_A \mathrm{d}y\,\mathrm{d}x$ thus specifically captures the effect of the slope-current encounter on energy dissipation. That is, it tells us how much EKE dissipation occurs as a result of slope-current interactions over a unit area on the anticyclonic side of the ridge. Wenegrat and

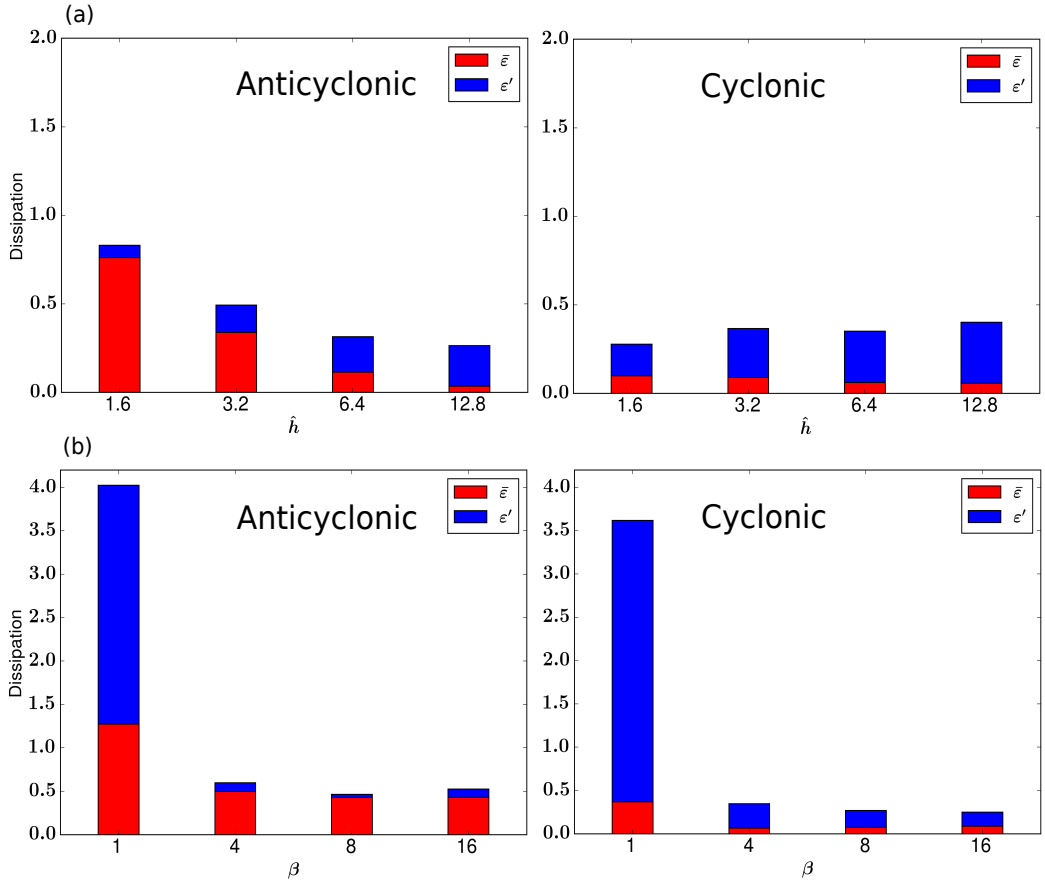

Figure 11. Barplot showing separate contributions of $\bar{\varepsilon}$ and ε', defined in Eqs. (25a) and (25b), to the energy dissipation on each side of the ridge. The integrals have been normalized by $C_d^* V_0^3$ with $C_d^* = 0.0022$, the usual scaling for the depth integrated dissipation rate in a turbulent BBL with far-field velocity V_0 (Sen et al., 2008; Arbic et al., 2009). (a) Elongated ridge with varying $\hat{h}$ and (b) Elliptical ridge at fixed $\hat{h} = 3.2$ and varying lateral aspect ratio $\beta = b/a$.

Thomas (2020) predicted using theoretical scalings that in a 2D downwelling BBL undergoing arrest, NPV instabilities offset exactly half of the *reduction* in the energy dissipation caused by Ekman arrest. Here we find that ε' on the anticyclonic side increases from around 0.05 at $\hat{h} = 1.6$ to around 0.2 at $\hat{h} = 12.8$. Thus while dissipation due to SI/CI amounts to between 5% and 20% of the expected flat-bottom BBL dissipation, it is nevertheless considerably smaller in our solutions compared to the Wenegrat and Thomas (2020) scaling.

On the cyclonic side, $\bar{\varepsilon}$ is below 0.1 for all $\hat{h}$ while ε' is around 0.3 at the largest $\hat{h}$. Thus dissipation resulting from the horizontal inflectional point instability outstrips that due to the bottom drag for all but the lowest $\hat{h}$ considered. In conclusion, on both sides of the ridge, EKE dis-

sipation compensates a fraction of the reduction in dissipation resulting from partial arrest of the turbulent BBL on the slopes — between 5% and 20% on the anticyclonic side and up to 30% on the cyclonic side, depending on the value of $\hat{h}$. Note that Fig. 11b shows the same fractional contributions to total dissipation, but for an elliptical ridge with varying lateral aspect ratio $\beta = b/a$, where a and b are respectively the half-length and half-width in the along- and cross-stream directions. These solutions will be discussed in detail in section 5.

An interesting question concerns the connection between form drag and wake dissipation, an issue recently explored by Puthan et al. (2022a) for tidally modulated topographic wakes. The form drag is a natural quantity in an integrated momentum balance and is defined as the decelerating force experienced by the barotropic flow due to the presence of topography $h(x,y)$. For the barotropic inflow $\mathbf{u} = V_0\hat{\mathbf{y}}$ ($\hat{\mathbf{y}}$ being the unit vector in the y direction) in our ridge configuration, it is given by the expression

$$\mathscr{F}_D = \int_{-\infty}^{+\infty}\int_{-\infty}^{+\infty} p_b \frac{\partial h}{\partial y}\mathrm{d}y\,\mathrm{d}x = \int_{-\infty}^{+\infty}\int_{-\infty}^{+\infty} h\frac{\partial p_b}{\partial y}\mathrm{d}y\,\mathrm{d}x, \tag{27}$$

where p_b denotes the pressure at the bottom. Note that form drag as such cannot do any work on the fluid flow in a volume integral sense because of the no-normal-flow condition on solid boundaries which renders the $p\boldsymbol{u}\cdot\hat{n}$ term in the volume-integrated energy equation, uniformly zero. However, as demonstrated in MacCready et al. (2003), form drag can, and does effect energy exchanges between the free stream and local flow near topography, which manifests as lee waves, eddies and dissipation. Table 1 shows the rate of work done by the time-averaged form drag $\overline{\mathscr{F}_D}V_0$ and the volume-integrated dissipation rate associated with the eddying flow along the slopes and in the wake region. Both these quantities are given in dimensional form for each of the $\hat{h}$ values considered. Dissipation comprises a small fraction of energy conversion by form drag. Since lee waves are negligible in these high $\hat{h}$ flows, our interpretation of this result is that the bulk of the work done by form drag is mainly expended on transferring energy from the incident flow V_0 to both the time mean and fluctuating components of the circulation around the ridge. The latter comprises eddies arising from NPV instabilities as well as flow separation, which advect downstream, manifesting as coherent wake vortices. The dissipation rate increases with $\hat{h}$, consistent with the findings in Srinivasan et al. (2021). We remark that in the presence of tides, there is an important subtlety in the interpretation of form-drag-work. Considering a background flow $V_b = V_c + V_t \sin\Omega_t t$, where V_c is the current speed, V_t the tidal flow amplitude and ω_t its frequency, Puthan et al. (2022a) note that the work expended by the time-averaged form drag $\overline{\mathscr{F}_D}V_c$ is distinct from the quantity $\overline{\mathscr{F}_D V_b}$ which includes energy conversion from the tides.

Table 1. Rate of work done by form drag on topography, $\mathscr{F}_D V_0$ along with corresponding volume integrated dissipation rate of TKE in the wake $\iiint_V \rho_0 \varepsilon' \, dV$, where $\varepsilon' = \overline{\boldsymbol{u'} \cdot \left(\boldsymbol{\tau}'_z + \mathscr{D}_H \boldsymbol{u'}\right)}$ is the component of energy dissipation associated with the eddying flow in the wake, $\mathscr{D}_H$ being the implicit horizontal hypervisous operator in ROMS.

$\hat{h}$	$\mathscr{F}_D V_0 (MW)$	$\iiint_V \varepsilon' \, dV (MW)$
1.6	7.8	0.63
3.2	7.41	1.09
6.4	6.87	1.26
12.8	6.05	1.46

A caveat to the above observations regarding NPV and dissipation concerns the horizontal resolution used (300 m). Note that locally, we can estimate the horizontal scale of symmetric instability modes from Taylor and Ferrari (2009) as

$$L = h_{bbl} / \theta_{iso}, \tag{28}$$

where θ_{iso} is the isopycnal slope within the BBL. In Fig. 12, we display the absolute values of the isopycnal slope on the anticyclonic side for the case $\hat{h} = 3.2$. Note that at $y/a = 27$, which is around where the NPV instabilities become prominent in snapshots of integrated vorticity (Fig. 1), $|\theta_{iso}|$ in the BBL is largely in the range of 0.1 or less, except very near the bottom where it approaches unity. The isopycnal slopes are very similar for the other $\hat{h}$ and hence not shown.

Substituting the values of V_0, $\hat{h}$ and N for our runs in Eq. 14 gives theoretical arrest heights ranging from $\approx$ 220 m for $\hat{h} = 1.6$, to $\approx$ 160 m for the $\hat{h} = 12.8$. From inspection of Fig. 10, this gives values of h_{bbl} before separation from the ridge, of around 165 m for $\hat{h} = 1.6$, 65 m for $\hat{h} = 12.8$ and around 90 m for each of the cases $\hat{h} = 3.2$ and 6.4. From Eq. (28), this implies a horizontal scale of the symmetric instability mode $L \approx 1650$ m for $\hat{h} = 1.6$, 900 m for $\hat{h} = 3.2$ and 6.4 and 650 m for the largest $\hat{h}$ of 12.8 considered here. Thus with a horizontal resolution of 300 m, our simulations capture the onset of symmetric instability, but do not resolve their evolution to finite amplitude and subsequent equilibriation via secondary Kelvin-Helmholtz instability (Taylor & Ferrari, 2009). Consequently it is likely that the dissipation rates obtained here underestimate the true rate of energy dissipation in hybrid NPV, particularly for large $\hat{h}$.

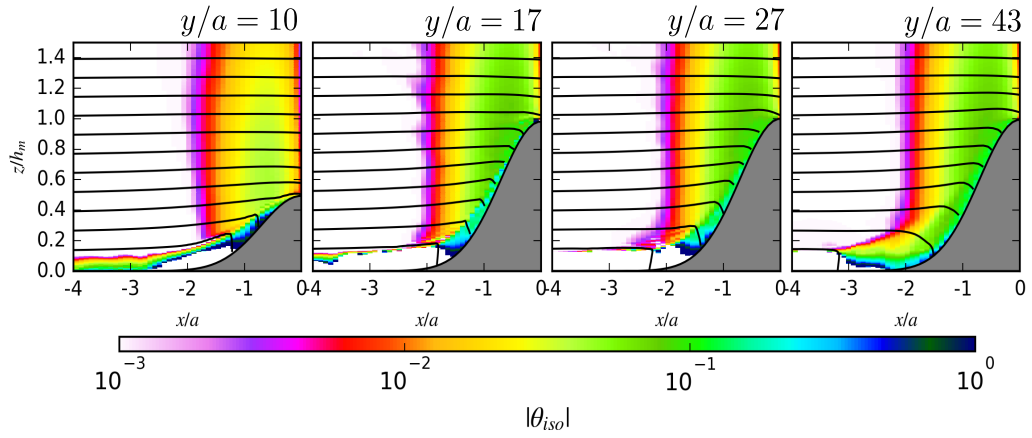

Figure 12. Downstream evolution of the time-averaged isopycnal slope $|\theta_{iso}|$ on the anticyclonic (downwelling) side where symmetric instability modes are present, for the $\hat{h} = 3.2$ solution.. Also overlain are the mean flow isopycnals. Note that, except very close to the boundary, $|\theta_{iso}|$ is largely $\mathcal{O}(0.1)$ or smaller adjacent to the ridge slope.

5 The effect of ridge curvature

The elongated ridge (Fig. 1) was specifically chosen for this study as it represents a particularly favorable configuration for observing 1D-like buoyancy adjustment in a 3D setting. With curvature and/or shorter ridge length, the evolution to Ekman arrest is expected to be vitiated by vortical dynamics and agesotrophic instabilities. To demonstrate how this may happen, we have performed additional simulations for elliptical ridges with varying lateral aspect ratio $\beta = b/a$, where a and b are respectively, the cross-flow and along-flow dimensions of the ridge. $\hat{h}$ is set to 3.2 in all these runs. This value of $\hat{h}$ is comparable to the observed value of $\hat{h}$ (≈ 3) over the seamounts of the Tokara strait lying in the path of the Kuroshio current (Nagai et al., 2021). Fig. 13 shows the time-averaged bottom stress and instantaneous snapshots of integrated vorticity for three cases corresponding to $\beta = 1$, 4 and 16. Compared to the elongated ridge (Fig. 1), the bottom stress here exhibits less of a systematic downstream pattern; rather stress reduction is patchy and spatially intermittent. As also seen in the former, bottom stress divergence torque (Jagannathan et al., 2021) acting on the slopes, generates vorticity, which upon flow separation leads to the emergence of highly coherent vortical wakes.

As we shall see below, for small-to-moderate aspect ratios β, the NPV instability on the anticyclonic side is dominated by centrifugal rather than symmetric modes, i.e. the NPV comes mainly from the vertical component of PV, $q_v = (\zeta + f)b_z$, where ζ is the relative vertical vor-

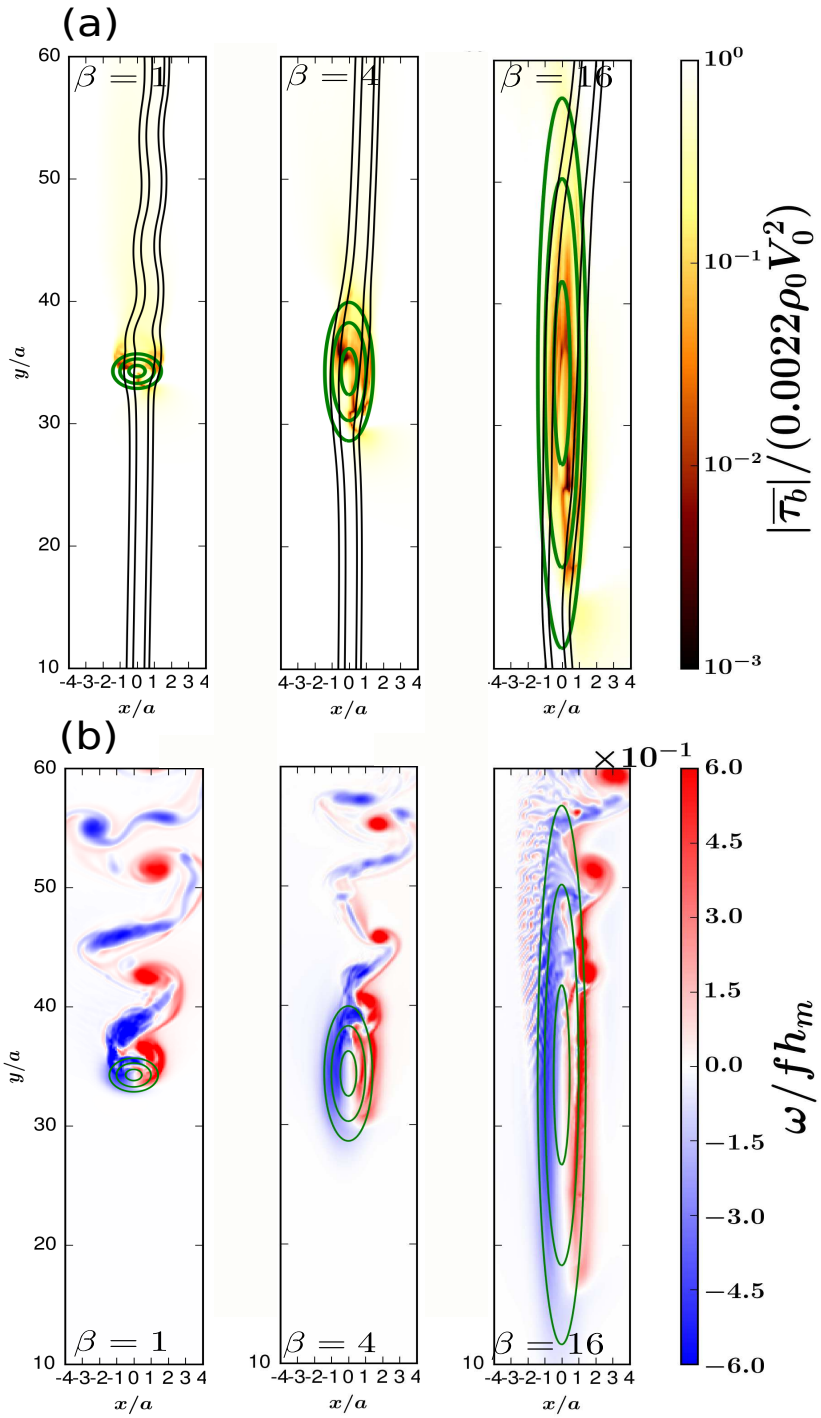

Figure 13. Same as Fig. 1 but for elliptical shaped ridges with varying aspect ratio β, at a fixed $\hat{h} = 3.2$. Note that the small scale eddying structures on the anticyclonic side for $\beta = 16$ case mirror similar structures seen in the case of the elongated ridge (Fig. 1)

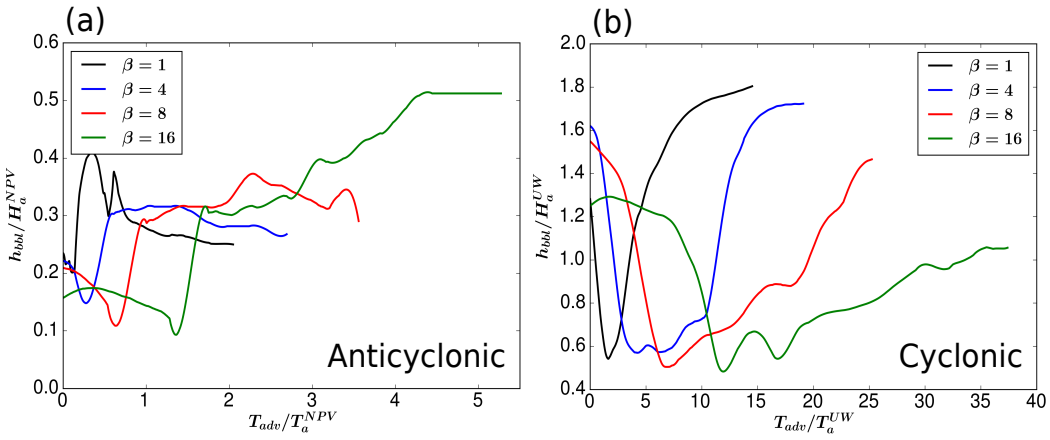

Figure 14. Same as Fig. 10 but for the elliptical ridge solutions. (a) Anticyclonic side and (b) Cyclonic side.

654 ticity. For this reason, the symmetric instability criterion of Allen and Newberger (1996) is not
655 the most appropriate choice for defining the BBL height for the elliptical ridge solutions. To en-
656 able consistent comparison between the different β cases, we instead define the BBL height here
657 as the depth over which the stratification is smaller than N^2. The downstream evolution of the
658 BBL height is shown in Fig. 14. For a circular ridge ($\beta = 1$), the encounter time along the slopes
659 is insufficient for sustained buoyancy adjustment to occur. For $\beta = 4$ and higher, the BBL on
660 the anticyclonic side deepens downstream following a sharp contraction during the initial encounter
661 with the ridge. The deepening BBL is evidence of convective mixing, similar to what occurs over
662 the elongated ridge (Fig. 10); this is particularly evident for the $\beta = 16$ case. On the cyclonic
663 side, the evolution of the BBL is similar in most respects to that observed over the elongated ridge
664 (Fig. 3). The BBL height shrinks on the slopes due to the stabilizing effect of upslope Ekman
665 transport as predicted in Brink and Lentz (2010a) and seen in Fig. 10 above. In all cases the BBL
666 subsequently rebounds toward its pre-encounter height.

667 A notable aspect of these solutions concerns the EKE production and dissipation on the
668 anticyclonic side. Fig. 15 reveals that the energy conversion terms are an order of magnitude larger
669 in the case of $\beta = 1$ compared to $\beta = 16$. Focussing on the anticyclonic side, EKE production
670 for $\beta = 1$ is predominantly due to HRS and occurs downstream of the ridge. Combined with the
671 fact that the anticyclonic eddies are associated with NPV anomalies, this is indicative of centrifu-
672 gal instability. By contrast, for $\beta = 16$, energy transfer from the mean flow to the eddies occurs
673 through a combination of HRS, VRS and VBF. Furthermore, VRS production in this case begins

on the slopes (Fig. 15), indicating that the instability emerges even as the BBL is evolving on the slopes. We identify this as a hybrid centrigual/symmetric/gravitational mode of instability, similar to that seen in the $\hat{h} = 3.2$ elongated ridge solution (Figs. 1,9). This hybrid mode is characterized by a smaller horizontal scale than the $\beta = 1$ solution, as is visually evident (e.g. in Fig. 13).

A direct consequence of the shifting EKE production patterns on the anticylonic side is on the zonally, and depth integrated dissipation rate of EKE $\int_{-\infty}^{0}\int_{-H}^{\eta}\overline{\boldsymbol{u'}\cdot\left(\boldsymbol{\tau}'_z+\mathscr{D}\boldsymbol{u'}\right)}\,\mathrm{d}z\mathrm{d}x$. As a function of aspect ratio, Fig. 16b shows that energy dissipation is highest for $\beta = 1$, decreases as β increases through to 8, and again increases for $\beta = 16$. For comparison, we note that the EKE dissipation rate in the elongated ridge solutions (Fig. 16a) exhibits a monotonic increasing trend with $\hat{h}$. We may interpret the trend in EKE dissipation observed in Fig. 16b using the EKE production terms shown in Fig. 15. Increasing the aspect ratio of the ridge from $\beta = 1$ to 8, there is a transition from a highly dissipative centrifugal instability to a more modestly disspative one. As the curvature decreases further (or the encounter length increases), there is more time for buoyancy adjustment to occur on the slopes. The resulting increase in the geostrophic vertical shear renders the flow unstable to a hybrid centrifugal/symmetric/gravitational mode which enhances turbulent dissipation. A related recent finding of interest (Chor et al., 2022) is that centrifugally dominated NPVs tend to have higher mixing efficiency, both instantaneous as well as cumulative, compared to symetrically dominated NPVs.

Notably, Fig. 16b shows that for all values of β considered, elevated levels of turbulent dissipation persist downstream over $\mathscr{O}(10)$ ridge width (a) scales. We note that this is consistent with recent turbulence microstructure measurements of Nagai et al. (2021) that reveal long pesisting (≈ 100 km wide) subsurface turbulence in the seamount wakes of the Tokara strait, whose origins the authors largely trace to NPV instabilities triggered by the flow of the Kuroshio past the steep seamount slopes.

The overall contribution of ε' to the total energy dissipation is highest for the circular ridge (Fig. 11b). The normalized total dissipation rate in this case is over 3.5 in an area-averaged sense, with bottom drag dissipation $\bar{\varepsilon}$ around 1.3 and 0.4 respectively on the anticyclonic and cyclonic sides — an indication that buoyancy adjustment effects are small. The bottom drag dissipation on the anticyclonic side is around 0.5 for $\beta = 4$ and higher and the total dissipation rate itself also remains below 1. This is roughly in line with the recent findings of Ruan, Wenegrat, and Gula (2021) who find that geostrophic shear in the BBL reduces energy dissipation by at least 56%

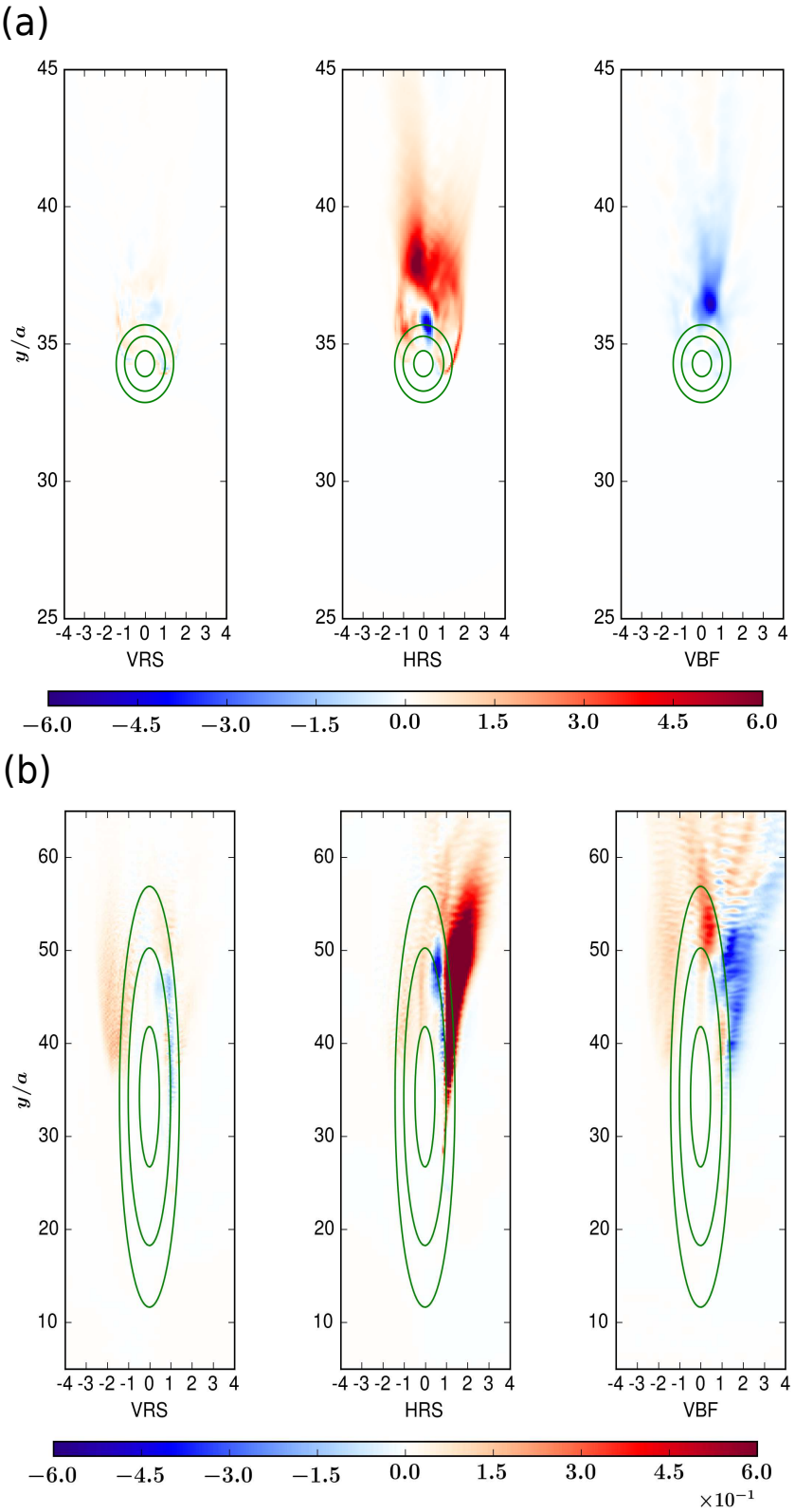

Figure 15. Same as Fig. 9 but for the ellliptical ridge solutions. (a) $\beta = 1$ and $\beta = 16$. The EKE production is much higher for $\beta = 1$; accordingly the colomap is saturated at 5×10^{-2} in (a) and 5×10^{-3} in (b).

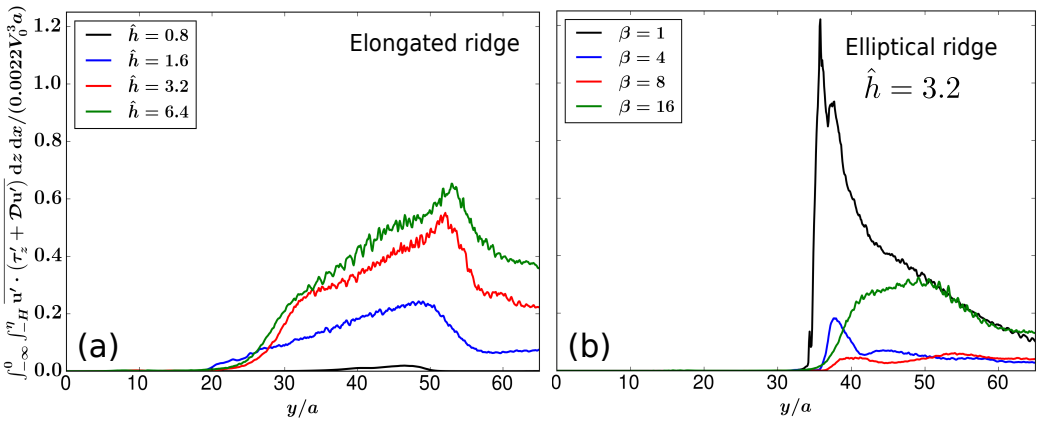

Figure 16. Downstream evolution of the zonally, and depth integrated dissipation rate $\int_{-\infty}^{0}\int_{-H}^{\eta}\overline{\boldsymbol{u}'\cdot\left(\boldsymbol{\tau}_z'+\mathscr{D}_H\boldsymbol{u}'\right)}\,\mathrm{d}z\,\mathrm{d}x$ of EKE corresponding to the eddying flow component on the anticyclonic side. (a) elongated ridge solutions at different values of $\hat{h}$ and (b) elliptical ridge solutions with varying β, at a fixed value of $\hat{h} = 3.2$. The values have been normalized by $C_d^* V_0^3 a$ with $C_d^* = 0.0022$, the expected dissipation rate within a turbulent BBL over a horizontal width a.

in a high-resolution model of the Atlantic. On the cyclonic side, the total dissipation rate ranges between 0.28 and 0.35 as β goes from 4 to 16 (Fig. 11b), energy loss due to bottom drag is diminished by as much as 90% relative to the flat bottom scaling and ε' comprises a much larger fraction of the total dissipation compared to the anticyclonic side.

6 Discussion

6.1 Temporal Vs spatial evolution of buoyancy adjustment

We have examined the process of bottom stress reduction and buoyancy adjustment within the BBL in a 3D setting of barotropic inflow encountering an elongated ridge. While the details of the ridge geometry and setup here may not be exactly representative of known oceanic flows, the rationale for choosing an elongated ridge is that it allows longer downstream/along-slope evolution of the BBL (before flow separation). So this is a natural configuration in which to investigate the question, 'how does the spatio-temporal BBL evolution and in particular, the buoyancy adjustment process in 3D, depart from the 1D expectation?'. Furthermore, the setup is general enough that our solutions and analysis can provide insight into the evolution of the BBL wherever boundary currents flow past continental shelf slopes, such as in the southwestern Pacific example discussed in section 2.2.).

In section 4.1, we analyzed the quasi-temporal evolution of the bottom stress along the slopes by defining an advective time scale T_{adv} and scaling this with T_a^{NPV} and T_a^{UW}. The implicit assumption behind this scaling was an approximate equivalence between the downstream evolution of the BBL along the ridge slopes, and temporal evolution in 1D and 2D (as in Brink & Lentz, 2010a; Wenegrat & Thomas, 2020). Using an idealized theoretical model with a linear bottom drag, Chapman and Lentz (1997) found that although this assumption does not strictly hold in the case of initially narrow currents, the evolution of a wide current over a sloping bottom is essentially 1D downstream, with along-isobath distance playing the role of time. Here we find that non-linear straining effects during the current-topographic encounter results in a rapid initial adjustment of the BBL and significant stress reduction over advective times $T_{adv} < T_a^{NPV}$ (Fig. 3c and Fig. 7). Further, the quadratic bottom drag in our simulations, instabilities, secondary circulations, and early flow separation (on the cyclonic side) mean that the evolution of the BBL in the downstream direction departs considerably from the expectation of quasi-temporal 1D evolution of Chapman and Lentz (1997).

6.2 Sensitivity to choice of BBL parameterization

Much of the previous work exploring buoyancy adjustment over slopes have utilized either a $k-\varepsilon$ closure (Brink & Lentz, 2010a), 2.0 or 2.5 level Mellor-Yamada closure (Brink & Lentz, 2010a; Benthuysen et al., 2015) for parameterizing BBL turbulence. Recently, LES have also been employed for this purpose (Ruan et al., 2019; Ruan, Thompson, & Taylor, 2021; Wenegrat & Thomas, 2020). Wijesekera et al. (2003) carried out a systematic comparison of $k-\varepsilon$, Mellor-Yamada 2.5 and KPP mixing in modelling the structure of vertical mixing over a continental shelf forced by either upwelling- or downwelling-favorable winds. Although they note some quantitative differences in the vertical profiles of eddy viscosity and diffusivity, the shape and structure of these mixing coefficients was similar across all three schemes, with local maxima in the surface and bottom boundary layers and a smooth connection to the interior. In particular, they find that all three models produce a similar BBL thickness and vertical profiles of velocity and density. In another study, Bachman et al. (2017) found that when the shear instability component of KPP is included, the total turbulence production compares favorably with LES solutions even though individual components may sometimes be overestimated. All the simulations here are performed with the shear instability component of KPP included and the critical Richardson number set to 0.45. Thus taking a statistical steady state view that turbulence pro-

duction must equal dissipation in a volume integral sense, KPP is unlikely to be a major source of error in our dissipation calculations.

6.3 Distinguishing Ekman arrest and turbulence collapse

In their LES solutions with periodic boundary conditions in the cross- and along- slope directions, Ruan et al. (2019); Ruan, Thompson, and Taylor (2021) observe that, both in the downslope and upslope regime, the BBL always relaminarizes before an arrested state is reached. This is a consequence of suppression of turbulence by the cross-slope buoyancy flux, a phenomenon which the authors characterize using a so-called slope-Obukhov length scale, defined as

$$L_s = \frac{-u_0^{*3}}{\kappa U_E N^2 \theta}. \tag{29}$$

In Eq. (29), θ is the slope angle and $U_E N^2 \theta$ is the cross-slope Ekman buoyancy flux. Given a molecular viscosity ν, Ruan et al. (2019); Ruan, Thompson, and Taylor (2021) find that turbulence collapse occurs when $L_s u^*/\nu$ falls below a threshold, around 100. However in the 2D solutions of Wenegrat and Thomas (2020), where both submesoscale instabilities and the near-wall layer are adequately resolved, the onset of NPV instabilities appears to prevent a relaminarized state from being attained.

As shown in Flores and Riley (2011), turbulence collapse occurs when there is insufficient scale-separation between the $\mathcal{O}(L)$ and $\mathcal{O}(\nu/u^*)$ scales of turbulent motions in the dynamic sublayer, where L is the Obukhov length and ν is the molecular viscosity. Here we do not expicitly resolve the dynamic sublayer, but rather rely on a turbulent bottom drag parameterization. Thus turbulence collapse in our solutions, if it occurs, would imply $u_0^* \to 0$. However since buoyancy adjustment itself leads to substantial reduction of the bottom stress, we note that it is difficult to distinguish Ekman arrest from turbulence collapse. Fully 3D LES or DNS solutions are needed to understand if and how BBL relaminarization manifests over 3D bottom topography. We note however that, because EKE production is enhanced on both sides of the ridge following the onset of NPV instabilities (anticyclonic) and barotropic (cyclonic) instability modes (Fig. 10 above and Fig. 16 of Jagannathan et al. (2021)), EKE suppresion as a proxy for identifying BBL relaminarization (as in Ruan et al. (2019), may not be as useful in 3D.

7 Summary and conclusion

We have examined the process of buoyancy adjustment on 3D topography by analyzing a set of idealized ROMS simulations of an initially uniform upstream flow past an elongated ridge

and elliptical ridges with varying lateral aspect ratio. Key metrics such as the extent of reduction of the bottom stress, the BBL height and the observed adjustment time scales are discussed in the context of the 1D and 2D Ekman arrest literature. BBL turbulence in our solutions is parameterized using the K-profile parameterization (KPP) and the 300 m horizontal resolution employed resolves submesoscale motions, including the onset of NPV instabilities on the anticyclonic side. Analyzing the EKE budget, we further diagnose the nature of the instabilities that develop over the course of the downstream BBL evolution on each side of the ridge, and the dissipation resulting thereof.

The evolution of the bottom stress in our solutions (Figs. 1 and 3) is to be contrasted with the 1D model runs of Brink and Lentz (2010a) and the more recent 2D simulations of Wenegrat and Thomas (2020) covering a range of slope Burger numbers. In their (constant-slope) solutions, buoyancy adjustment effects inexorably push the bottom stress towards zero. This occurs over a time scale corresponding to the time of mixed layer growth, either through upright or slantwise convection. For the $\hat{h}$ values considered, the predicted arrest time scale T_a^{NPV} in Eq. (13) for a constant slope, ranges from 4 to 8 inertial periods for $\hat{h} = 12.8$ and 1.6 respectively, with the smallest theoretical arrest time scale corresponding to the largest $\hat{h}$ and vice-versa. Although there is a significant reduction of the stress on the slopes over these time scales (Fig. 3), analysis of the vertical shear equation shows that, contrary to 1D and 2D solutions where the stress reduction is purely due to the thermal wind shear induced by cross-slope buoyancy advection, here 3D nonlinear straining effects during the early encounter have an important role in the adjustment process.

The state of the BBL before separation, in the elongated ridge solutions, is characterized by suppression of the bottom stress by between 60% ($\hat{h} = 1.6$) to 95% ($\hat{h} = 12.8$) on the anticyclonic side with respect to the upstream flat-bottom value (Fig. 3a,c), and up to 80% reduction on the cyclonic side (Fig. 3b,d) for all $\hat{h}$. On the anticyclonic side, the stress has either plateaued or is decaying only slowly when the current separates (Fig. 3a,c). This is possibly due to the influence of secondary circulations that feedback into the interior along-slope flow, as was noted in Benthuysen et al. (2015). The depth of the BBL on the anticyclonic side also remains well below the 2D prediction of Wenegrat and Thomas (2020). On the cyclonic side, early separation reverses the decaying trend of bottom stress within a short distance downstream of the encounter (Fig. 3b,d). Thus on either side of the ridge, we may characterize the BBL as being in a state of 'partial arrest'.

Our solutions demonstrate an inverse relationship between the drag-mediated energy dissipation rate and non-dimensional ridge height $\hat{h}$ as well as lateral aspect ratio β (Fig. 11) — a consequence of increasing geostrophic BBL shear and reduced near-bottom velocities. This reduction in the bottom drag dissipation is somewhat compensated by dissipation arising from ageostrophic instabilities on either side, but to a lesser extent than predicted by Wenegrat and Thomas (2020). The exception is the circular ridge ($\beta = 1$) solution (Figs. 11b,16b) where the dissipation on both sides is significantly enhanced relative to the flat bottom BBL.

The fact that the bottom stress, energy dissipation and Ekman transport weaken substantially on the slopes of the ridge (Figs. 1 and 4) would suggest that partial Ekman arrest may be a fairly common occurence in boundary currents adjacent to the continental shelf. Yet oceanic observations of Ekman arrest remain scarce, a notable exception being the Northern California Shelf observations of Lentz and Trowbridge (2001). One possible explantion for this is that, on realistic bathymetry, curvature and irregular, small scale features such as headlands and bumps could trigger localized flow separation and reattachment events. This can be seen in the California Undercurrent (CUC). For example, Fig. 5 of Molemaker et al. (2015) shows eddies roll up and separate all along the coast, but especially around Point Sur. If such events sporadically punctuate the flow evolution on the slopes, they could potentially undermine the buoyancy adjustment process. Another plausible explanation for the paucity of observational data showing Ekman arrest, is the intrinsic temporal variability in the real ocean due to tides, wind-variability, coastally trapped waves and eddies impinging from offshore. In a 1D model with realistic broadband forcing, Brink and Lentz (2010b) find that the steady component of the flow undergoes Ekman arrest over time scales consistent with Eqs. (10) and (17), and further that the bottom stress is also reduced across nearly all frequencies. Further studies with a well-resolved BBL are needed to understand how 3D effects like curvature, alongshore advection and realistic forcing influence the dynamics of Ekman adjustment in oceanic boundary currents.

Acknowledgments

This work was made possible by the Office of Naval Research grant N00014-18-1-2599. Computing support was provided by the Extreme Science and Engineering Discovery Environment (XSEDE), which is supported by National Science Foundation grant number ACI-1548562. ALS was supported by the National Science Foundation under Grant Number OCE-1751386.

Data Availability Statement

The numerical model simulations upon which this study is based are too large to archive or to transfer. Instead, we provide all the information needed to replicate the simulations; we used the hydrostatic UCLA version of the Regional Ocean Modelling System (ROMS) to perform the simulations. The model code, compilation script, initial and boundary condition files, and the namelist settings are available at https://github.com/arjunj87/ROMS-ridge-solutions.

References

Allen, J., & Newberger, P. (1996). Downwelling circulation on the oregon continental shelf. part i: Response to idealized forcing. *J. Phys. Oceanogr.*, *26*(10), 2011–2035.

Arbic, B. K., Shriver, J. F., Hogan, P. J., Hurlburt, H. E., McClean, J. L., Metzger, E. J., ... Wallcraft, A. J. (2009). Estimates of bottom flows and bottom boundary layer dissipation of the oceanic general circulation from global high-resolution models. *J. Geophys. Res: Oceans*, *114*(C2).

Armi, L. (1978). Some evidence for boundary mixing in the deep ocean. *J. Geophys. Res.: Oceans*, *83*, 1971–1979.

Armi, L., & D'Asaro, E. (1980). Flow structures of the benthic ocean. *J. Geophys. Res.: Oceans*, *85*(C1), 469–484.

Armi, L., & Millard Jr, R. C. (1976). The bottom boundary layer of the deep ocean. *J. Geophys. Res.*, *81*, 4983–4990.

Bachman, S. D., Fox-Kemper, B., Taylor, J. R., & Thomas, L. N. (2017). Parameterization of frontal symmetric instabilities. i: Theory for resolved fronts. *Ocean Modell.*, *109*, 72–95.

Benthuysen, J., Thomas, L. N., & Lentz, S. J. (2015). Rapid generation of upwelling at a shelf break caused by buoyancy shutdown. *J. Phys. Oceanogr.*, *45*(1), 294–312.

Brink, K. H., & Lentz, S. J. (2010a, Jan). buoyancy arrest and bottom ekman transport. part I: Steady flow. *J.Phys. Oceanogr.*, *40*(4), 621–635.

Brink, K. H., & Lentz, S. J. (2010b, Dec). buoyancy arrest and bottom ekman transport. part II: Oscillating flow. *J. Phys. Oceanogr.*, *40*(4), 636–655.

Chang, M.-H., Tang, T. Y., Ho, C.-R., & Chao, S.-Y. (2013). Kuroshio-induced wake in the lee of green island off taiwan. *J. Geophys. Res. : Oceans*, *118*(3), 1508–1519.

Chapman, D. C., & Lentz, S. J. (1997). Adjustment of stratified flow over a sloping bottom. *J. Phys. Oceanogr.*, *27*(2), 340–356.

Chor, T., Wenegrat, J. O., & Taylor, J. (2022). Insights into the mixing efficiency of submesoscale centrifugal–symmetric instabilities. *J. Phys. Oceanogr.*, *52*(10), 2273–2287.

Flores, O., & Riley, J. (2011). Analysis of turbulence collapse in the stably stratified surface layer using direct numerical simulation. *Bound.-Layer Meteorol.*, *139*(2), 241–259.

Garabato, A. C. N., Frajka-Williams, E. E., Spingys, C. P., Legg, S., Polzin, K. L., Forryan, A., ... others (2019). Rapid mixing and exchange of deep-ocean waters in an abyssal boundary current. *Proc. Natl. Acad. Sci.*, *116*(27), 13233–13238.

Garrett, C., MacCready, P., & Rhines, P. (1993). Boundary mixing and arrested ekman layers: Rotating stratified flow near a sloping boundary. *Annu. Rev. Fluid Mech.*, *25*(1), 291–323.

Gula, J., Molemaker, M., & McWilliams, J. (2015). Topographic vorticity generation, submesoscale instability and vortex street formation in the gulf stream. *Geophys. Res. Lett.*, *42*(10), 4054–4062.

Hogg, N. G. (1973). On the stratified taylor column. *J. Fluid Mech.*, *58*(3), 517–537.

Hsu, P.-C., Cheng, K.-H., Jan, S., Lee, H.-J., & Ho, C.-R. (2019). Vertical structure and surface patterns of green island wakes induced by the kuroshio. *Deep Sea Res. Part I: Oceanographic Research Papers*, *143*, 1–16.

Jagannathan, A., Srinivasan, K., McWilliams, J. C., Molemaker, M. J., & Stewart, A. L. (2021). Boundary-layer-mediated vorticity generation in currents over sloping bathymetry. *J. Phys. Oceanogr.*, *51*(6), 1757–1778.

Jagannathan, A., Winters, K. B., & Armi, L. (2019). Stratified flows over and around long dynamically tall mountain ridges. *J. Atmos. Sci.*, *76*(5), 1265-1287.

Large, W. G., McWilliams, J. C., & Doney, S. C. (1994). Oceanic vertical mixing: A review and a model with a nonlocal boundary layer parameterization. *Rev. Geophys.*, *32*(4), 363–403.

Lentz, S., & Trowbridge, J. (2001). A dynamical description of fall and winter mean current profiles over the northern california shelf. *J. Phys. Oceanogr.*, *31*(4), 914–931.

MacCready, P., Pawlak, G., Edwards, K., & McCabe, R. (2003). Form drag on ocean flows. In *Near boundary processes and their parameterization: Proc. 13th'aha huliko'a hawaiian winter workshop* (pp. 119–130).

MacCready, P., & Rhines, P. B. (1991). Buoyant inhibition of ekman transport on a slope and its effect on stratified spin-up. *J. Fluid Mech.*, *223*, 631–661.

MacKinnon, J. A., Alford, M. H., Voet, G., Zeiden, K. L., Shaun Johnston, T., Siegelman,

M., ... Merrifield, M. (2019). Eddy wake generation from broadband currents near palau. *J. Geophys. Res.: Oceans*, *124*(7), 4891–4903.

McWilliams, J. C., Huckle, E., & Shchepetkin, A. F. (2009). Buoyancy effects in a stratified ekman layer. *J. Phys. Oceanogr.*, *39*(10), 2581–2599.

Molemaker, M. J., McWilliams, J. C., & Dewar, W. K. (2015). Submesoscale instability and generation of mesoscale anticyclones near a separation of the california undercurrent. *J. Phys. Oceanogr.*, *45*(3), 613–629.

Nagai, T., Hasegawa, D., Tsutsumi, E., Nakamura, H., Nishina, A., Senjyu, T., ... Tandon, A. (2021). The kuroshio flowing over seamounts and associated submesoscale flows drive 100-km-wide 100-1000-fold enhancement of turbulence. *Commun. Earth Environ.*, *2*(1), 170.

Orlanski, I. (1976). A simple boundary condition for unbounded hyperbolic flows. *J. Comput. Phys.*, *21*(3), 251–269.

Perfect, B., Kumar, N., & Riley, J. (2018). Vortex structures in the wake of an idealized seamount in rotating, stratified flow. *Geophys. Res. Lett.*, *45*(17), 9098–9105.

Perfect, B., Kumar, N., & Riley, J. (2020a). Energetics of seamount wakes. part I: Energy exchange. *J. Phys. Oceanogr.*, *50*(5), 1365–1382.

Perfect, B., Kumar, N., & Riley, J. (2020b). Energetics of seamount wakes. part II: Wave fluxes. *J. Phys. Oceanogr.*, *50*(5), 1383–1398.

Puthan, P., Pawlak, G., & Sarkar, S. (2022a). High drag states in tidally modulated stratified wakes. *J. Phys. Oceanogr.*, *52*(6), 1033–1048.

Puthan, P., Pawlak, G., & Sarkar, S. (2022b). Wake vortices and dissipation in a tidally modulated flow past a three-dimensional topography. *J. Phys. Oceanogr.*, *127*(8), e2022JC018470.

Ruan, X., Thompson, A. F., & Taylor, J. R. (2019). The evolution and arrest of a turbulent stratified oceanic bottom boundary layer over a slope: Downslope regime. *J. Phys. Oceanogr.*, *49*(2), 469–487.

Ruan, X., Thompson, A. F., & Taylor, J. R. (2021). The evolution and arrest of a turbulent stratified oceanic bottom boundary layer over a slope: Upslope regime and pv dynamics. *J. Phys. Oceanogr.*.

Ruan, X., Wenegrat, J. O., & Gula, J. (2021). Slippery bottom boundary layers: the loss of energy from the general circulation by bottom drag. *Geophys. Res. Lett.*, e2021GL094434.

Schär, C., & Davies, H. C. (1988). Quasi-geostrophic stratified flow over isolated finite amplitude topography. *Dyn. Atmos. Oceans*, *11*(3-4), 287–306.

Sen, A., Scott, R. B., & Arbic, B. K. (2008). Global energy dissipation rate of deep-ocean low-frequency flows by quadratic bottom boundary layer drag: Computations from current-meter data. *Geophys. Res. Lett.*, *35*(9).

Shchepetkin, A. F., & McWilliams, J. C. (2003). A method for computing horizontal pressure-gradient force in an oceanic model with a nonaligned vertical coordinate. *J. Geophys. Res.: Oceans*, *108*(C3).

Shchepetkin, A. F., & McWilliams, J. C. (2005). The regional oceanic modeling system (roms): a split-explicit, free-surface, topography-following-coordinate oceanic model. *Ocean Modell.*, *9*(4), 347–404.

Smolarkiewicz, P. K., & Rotunno, R. (1989). Low froude number flow past three-dimensional obstacles. part I: Baroclinically generated lee vortices. *J. Atmos. Sci.*, *46*(8), 1154–1164.

Srinivasan, K., McWilliams, J. C., & Jagannathan, A. (2021). High vertical shear and dissipation in equatorial topographic wakes. *J. Phys. Oceanogr.*, *51*(6), 1985–2001.

Srinivasan, K., McWilliams, J. C., Molemaker, M. J., & Barkan, R. (2019). Submesoscale vortical wakes in the lee of topography. *J. Phys. Oceanogr.*, *49*(7), 1949–1971.

Srinivasan, K., McWilliams, J. C., Renault, L., Hristova, H. G., Molemaker, J., & Kessler, W. S. (2017). Topographic and mixed layer submesoscale currents in the near-surface southwestern tropical pacific. *J. Phys. Oceanogr.*, *47*(6), 1221–1242.

St. Laurent, L., Ijichi, T., Merrifield, S. T., Shapiro, J., & Simmons, H. L. (2019). Turbulence and vorticity in the wake of palau. *Oceanogr.*, *32*(4), 102–109.

Taylor, J. R., & Ferrari, R. (2009). On the equilibration of a symmetrically unstable front via a secondary shear instability. *J. Fluid Mech.*, *622*, 103–113.

Taylor, J. R., & Sarkar, S. (2008). Stratification effects in a bottom ekman layer. *J. Phys. Oceanogr.*, *38*(11), 2535–2555.

Thomas, L. N., Taylor, J. R., Ferrari, R., & Joyce, T. M. (2013). Symmetric instability in the gulf stream. *Deep Sea Res. Part II: Topical Studies in Oceanography*, *91*, 96–110.

Trowbridge, J., & Lentz, S. (1991). Asymmetric behavior of an oceanic boundary layer above a sloping bottom. *J. Phys. Oceanogr.*, *21*(8), 1171–1185.

Umlauf, L., Smyth, W. D., & Moum, J. N. (2015). Energetics of bottom ekman layers during buoyancy arrest. *J. Phys. Oceanogr.*, *45*(12), 3099–3117.

970 Wang, P., McWilliams, J. C., & Ménesguen, C. (2014). Ageostrophic instability in rotating,
971 stratified interior vertical shear flows. *J. Fluid Mech.*, *755*, 397–428.
972 Wenegrat, J. O., & Thomas, L. N. (2020). Centrifugal and symmetric instability during ek-
973 man adjustment of the bottom boundary layer. *J. Phys. Oceanogr.*, *50*(6), 1793–1812.
974 Wenegrat, J. O., Thomas, L. N., Gula, J., & McWilliams, J. C. (2018). Effects of the sub-
975 mesoscale on the potential vorticity budget of ocean mode waters. *J. Phys. Oceanogr.*,
976 *48*(9), 2141–2165.
977 Wijesekera, H., Allen, J. S., & Newberger, P. (2003). Modeling study of turbulent mixing
978 over the continental shelf: Comparison of turbulent closure schemes. *J. Geophys. Res.*
979 *: Oceans*, *108*(C3).
980 Wunsch, C., & Ferrari, R. (2004). Vertical mixing, energy, and the general circulation of the
981 oceans. *Annu. Rev. Fluid Mech.*, *36*, 281–314.
982 Zeiden, K. L., Rudnick, D. L., MacKinnon, J. A., Hormann, V., & Centurioni, L. (2022).
983 Vorticity in the wake of palau from lagrangian surface drifters. *J. Phys. Oceanogr.*,
984 *52*(9), 2237–2255.

Figure1.

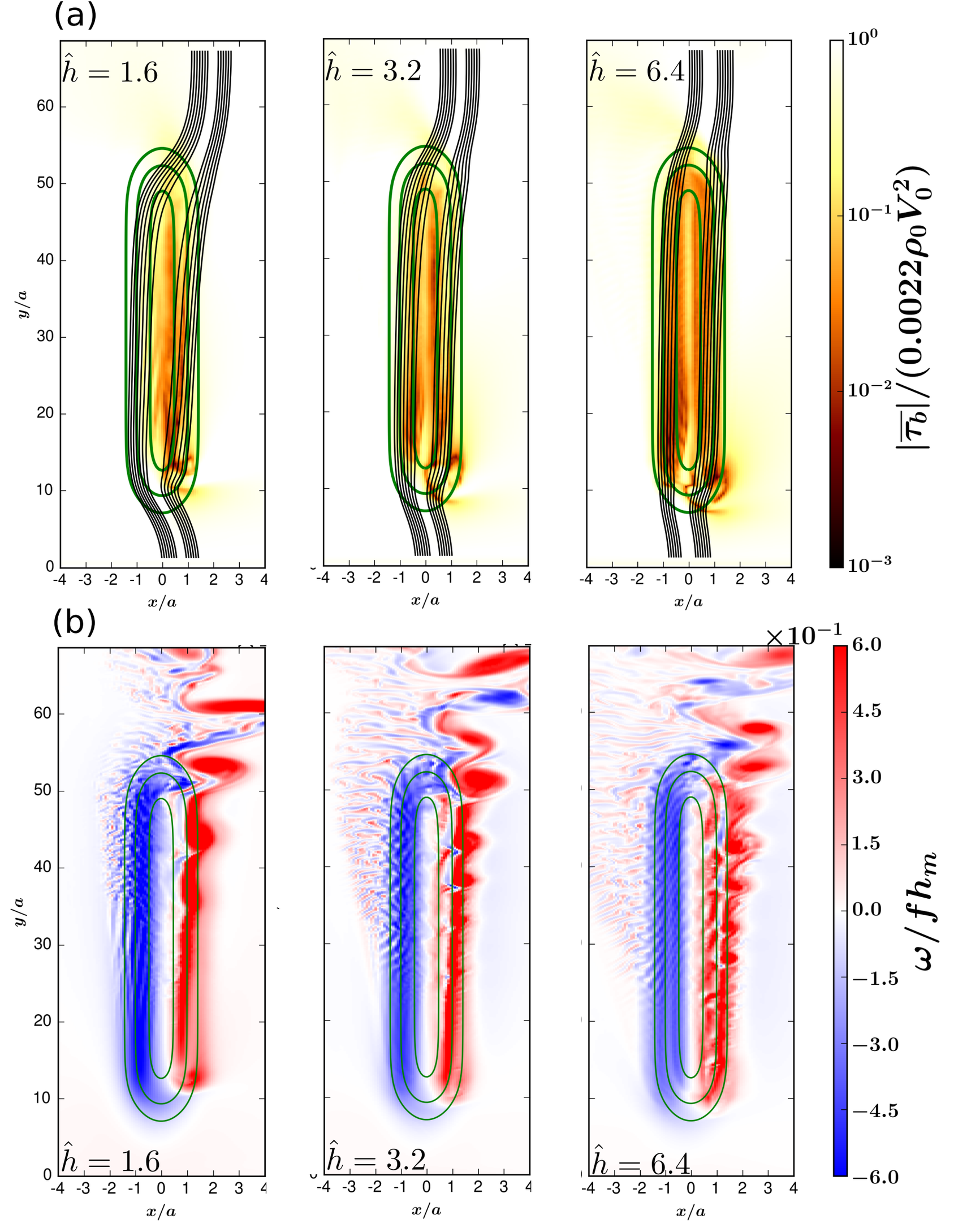
(a)
$\hat{h} = 1.6$
$\hat{h} = 3.2$
$\hat{h} = 6.4$
y/a
x/a
10^0
10^{-1}
10^{-2}
10^{-3}
$|\overline{\tau_b}|/(0.0022\rho_0 V_0^2)$
(b)
$\times 10^{-1}$
6.0
4.5
3.0
1.5
0.0
−1.5
−3.0
−4.5
−6.0
ω/fh_m

Figure2.

(a)

$10^\circ S$

$20^\circ S$

$150^\circ E$

$160^\circ E$

$10^\circ S$

$20^\circ S$

$145^\circ E$

$150^\circ E$

$155^\circ E$

0.5

0.4

0.3

0.2

0.1

0.0

$|\overline{U}|(ms^{-1})$

10^{-1} 10^{0} 10^{1} 10^{2}

$\overline{N}|\nabla h|/f$

(b)

(c)

Papua New Guinea

Solomon Sea

Gulf of Papua

Coral Sea

$10^\circ S$

$20^\circ S$

$150^\circ E$

$160^\circ E$

10^{-6} 10^{-5} 10^{-4} 10^{-3} 10^{-2} 10^{-1}

$|\overline{\tau_b}|/\rho_0(m^2s^{-2})$

$150^\circ E$

$160^\circ E$

-5 −4 −3 −2 −1 0 1 2 3 4 5

$\omega/f\langle D\rangle$ $\times 10^{-1}$

Figure3.

Anticyclonic

Cyclonic

(a)

(b)

(c)

(d)

$\hat{h} = 1.6$

$\hat{h} = 3.2$

$\hat{h} = 6.4$

$\hat{h} = 12.8$

$|\overline{\tau_b}|/(C_d\rho_0 V_0^2)$

s/a

T_{adv}/T_a^{NPV}

T_{adv}/T_a^{UW}

Figure4.

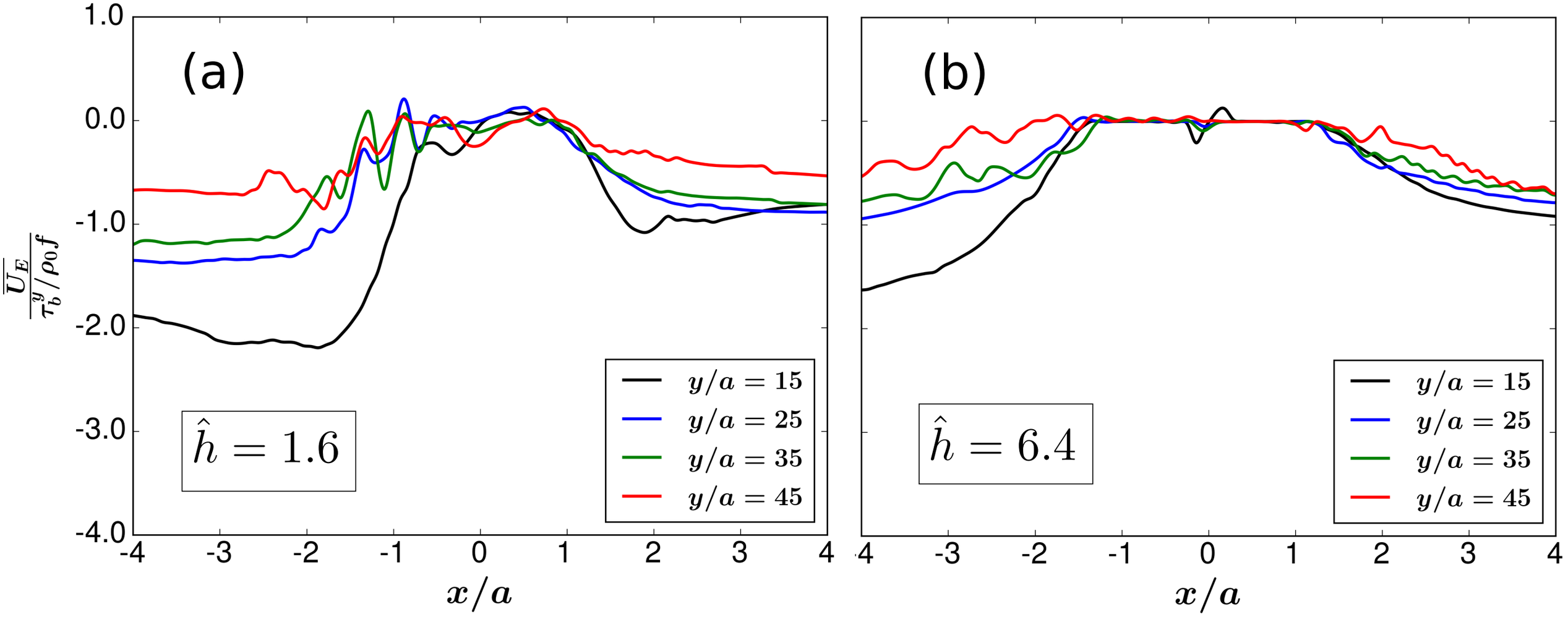
(a)
(b)
$\hat{h} = 1.6$
$\hat{h} = 6.4$
$y/a = 15$
$y/a = 25$
$y/a = 35$
$y/a = 45$
$\frac{\overline{U_E}}{\tau_b^y/\rho_0 f}$
x/a
1.0
0.0
-1.0
-2.0
-3.0
-4.0
-4
-3
-2
-1
0
1
2
3
4

Figure5.

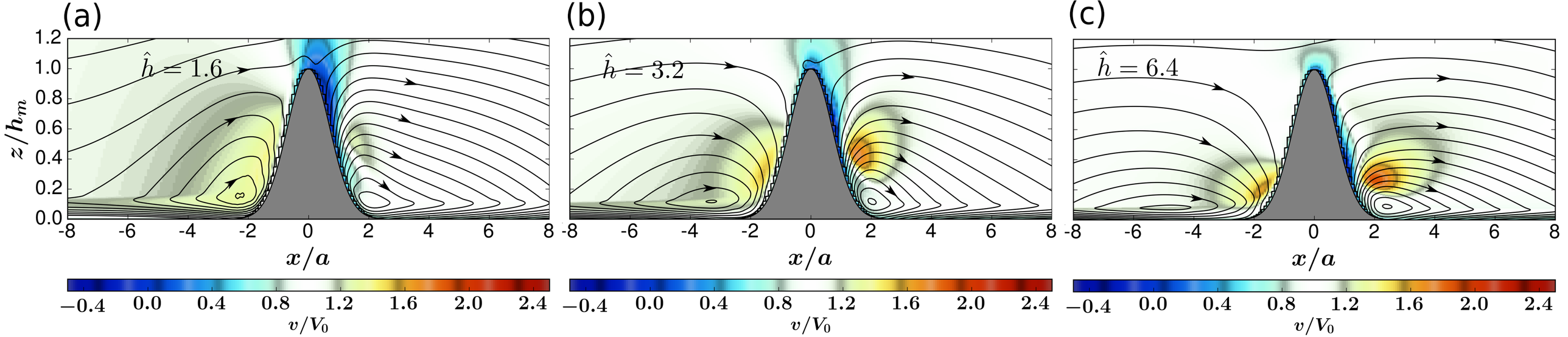
(a)
(b)
(c)
$\hat{h} = 1.6$
$\hat{h} = 3.2$
$\hat{h} = 6.4$
z/h_m
x/a
v/V_0
1.2
1.0
0.8
0.6
0.4
0.2
0.0
-8
-6
-4
-2
0
2
4
6
8
−0.4
0.0
0.4
0.8
1.2
1.6
2.0
2.4

Figure6.

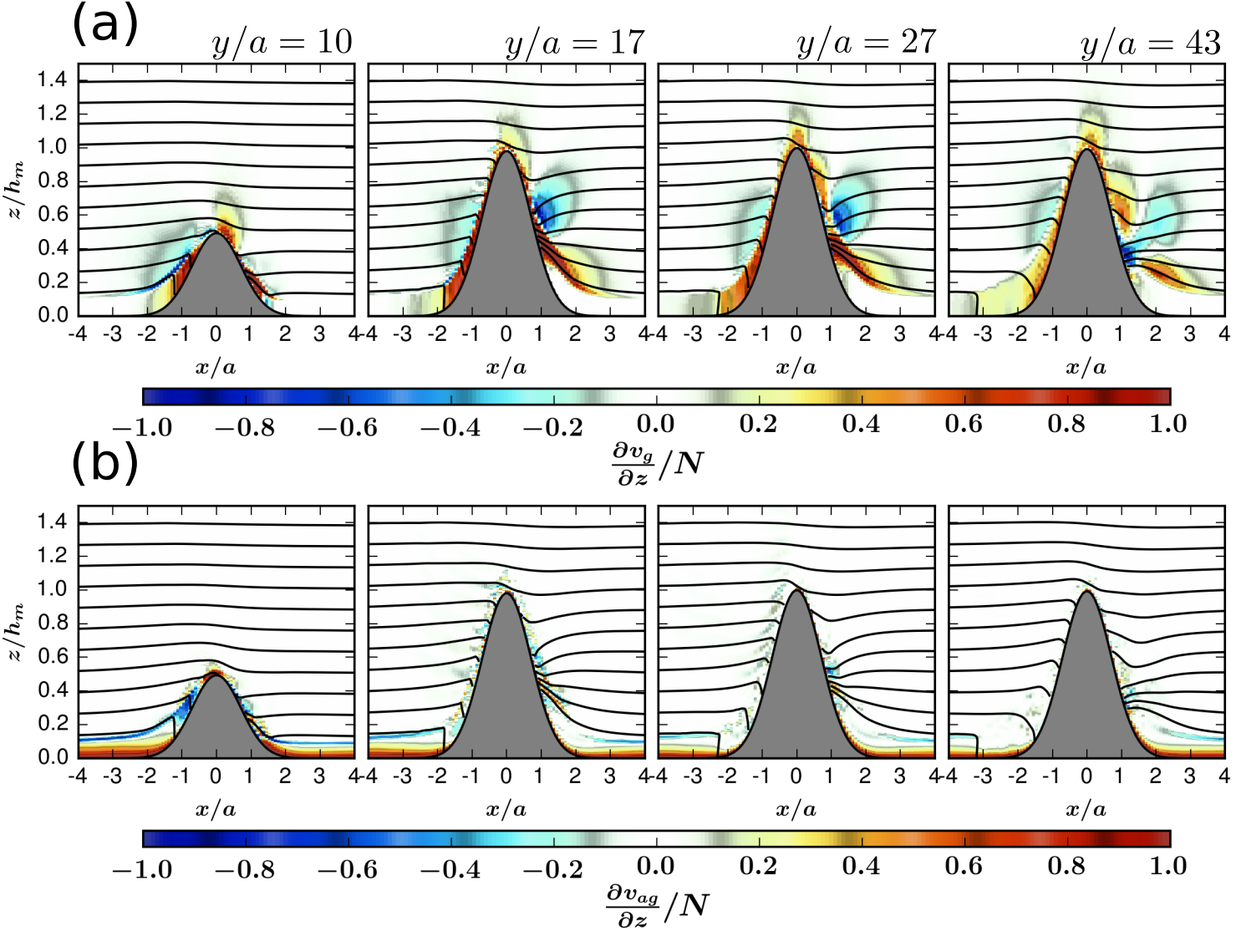
(a)
$y/a = 10$
$y/a = 17$
$y/a = 27$
$y/a = 43$
z/h_m
x/a
$\frac{\partial v_g}{\partial z}/N$
(b)
$\frac{\partial v_{ag}}{\partial z}/N$

Figure7.

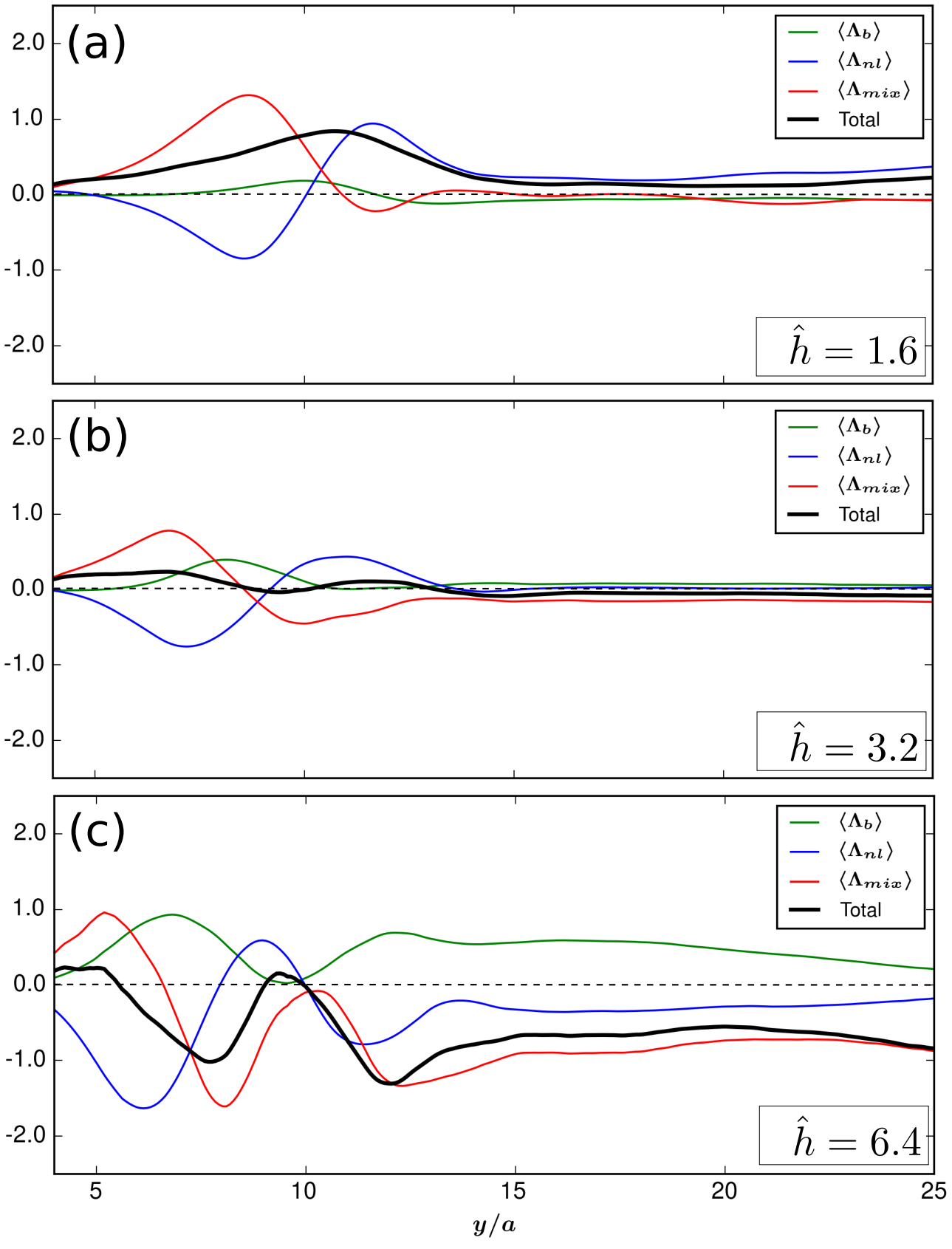
(a)
(b)
(c)
$\langle \Lambda_b \rangle$
$\langle \Lambda_{nl} \rangle$
$\langle \Lambda_{mix} \rangle$
Total
$\hat{h} = 1.6$
$\hat{h} = 3.2$
$\hat{h} = 6.4$
2.0
1.0
0.0
-1.0
-2.0
5
10
15
20
25
y/a

Figure8.

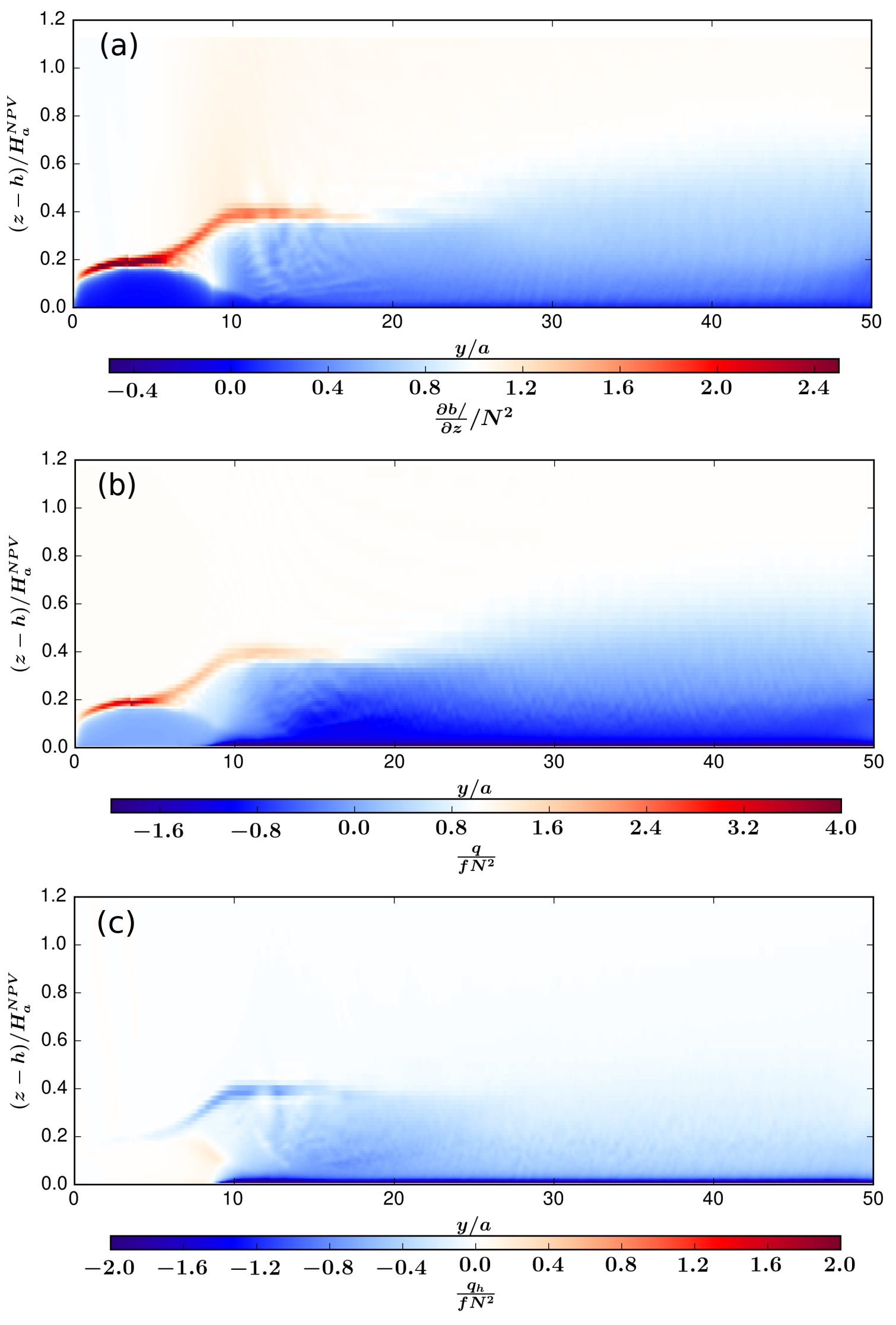
(a)
$(z-h)/H_a^{NPV}$
1.2
1.0
0.8
0.6
0.4
0.2
0.0
0
10
20
30
40
50
y/a
-0.4 0.0 0.4 0.8 1.2 1.6 2.0 2.4
$\frac{\partial b/}{\partial z}/N^2$
(b)
$(z-h)/H_a^{NPV}$
y/a
-1.6 -0.8 0.0 0.8 1.6 2.4 3.2 4.0
$\frac{q}{fN^2}$
(c)
$(z-h)/H_a^{NPV}$
y/a
-2.0 -1.6 -1.2 -0.8 -0.4 0.0 0.4 0.8 1.2 1.6 2.0
$\frac{q_h}{fN^2}$

Figure9.

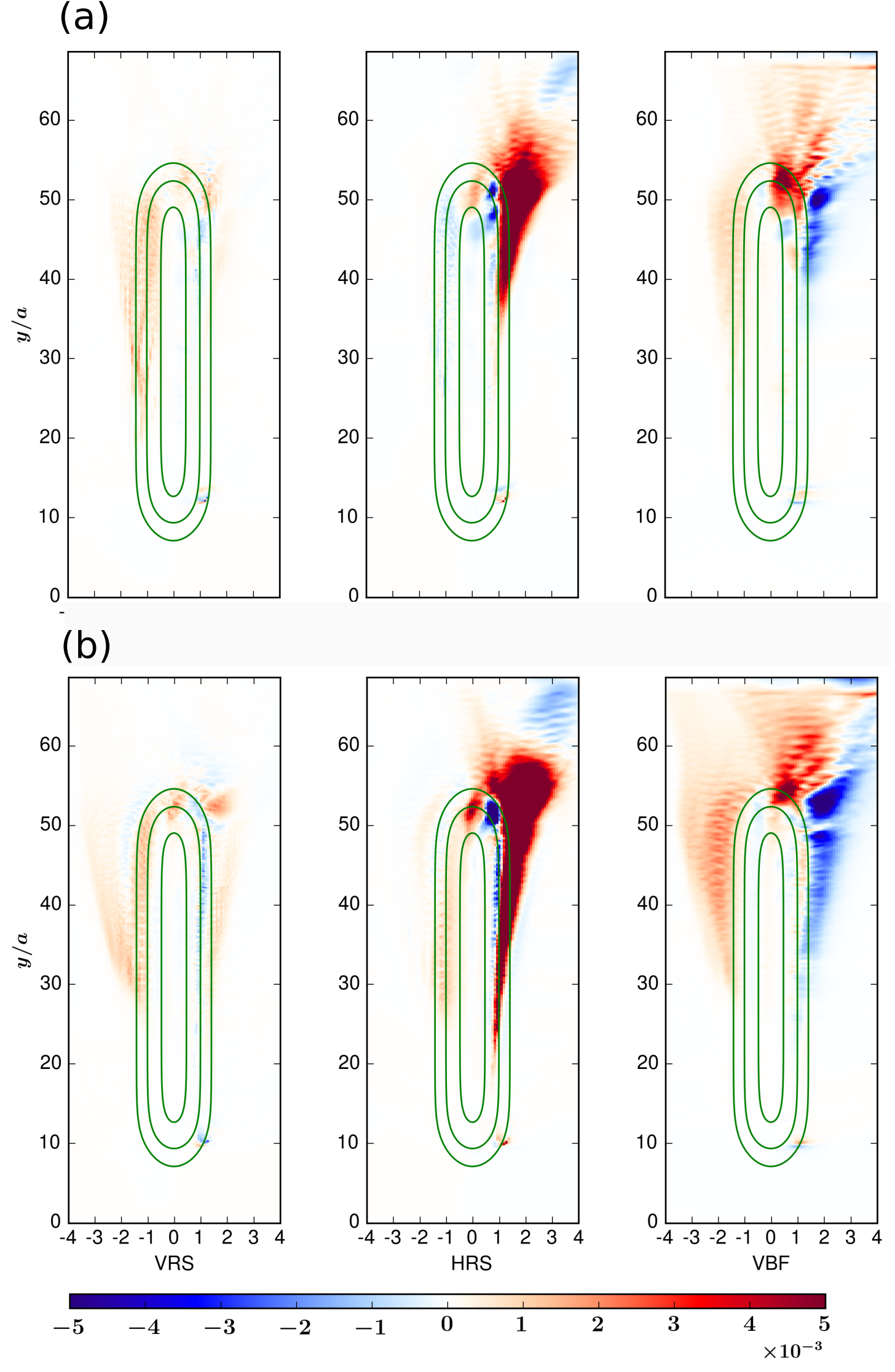
(a)
(b)
y/a
0
10
20
30
40
50
60
-4 -3 -2 -1 0 1 2 3 4
VRS
HRS
VBF
−5 −4 −3 −2 −1 0 1 2 3 4 5
×10−3

Figure10.

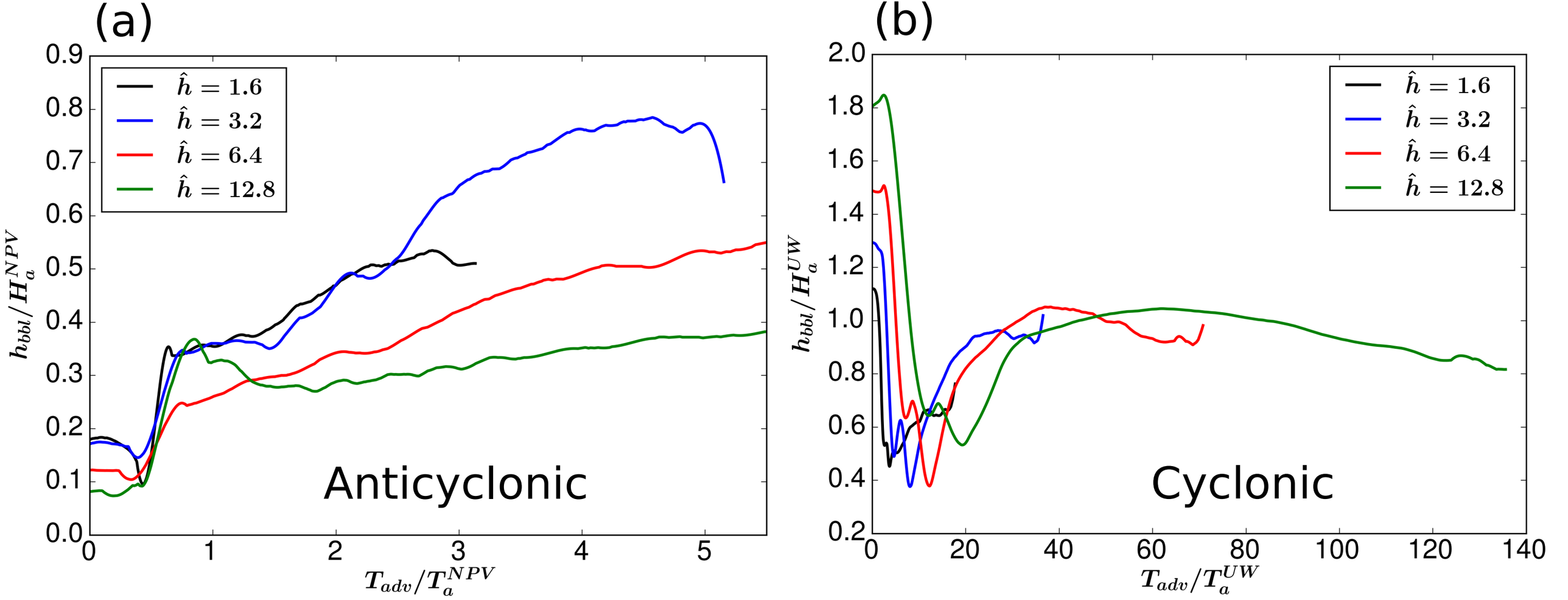
(a)
$\hat{h} = 1.6$
$\hat{h} = 3.2$
$\hat{h} = 6.4$
$\hat{h} = 12.8$
Anticyclonic
h_{bbl}/H_a^{NPV}
T_{adv}/T_a^{NPV}
0.0
0.1
0.2
0.3
0.4
0.5
0.6
0.7
0.8
0.9
0
1
2
3
4
5
(b)
$\hat{h} = 1.6$
$\hat{h} = 3.2$
$\hat{h} = 6.4$
$\hat{h} = 12.8$
Cyclonic
h_{bbl}/H_a^{UW}
T_{adv}/T_a^{UW}
0.2
0.4
0.6
0.8
1.0
1.2
1.4
1.6
1.8
2.0
0
20
40
60
80
100
120
140

Figure11.

(a)

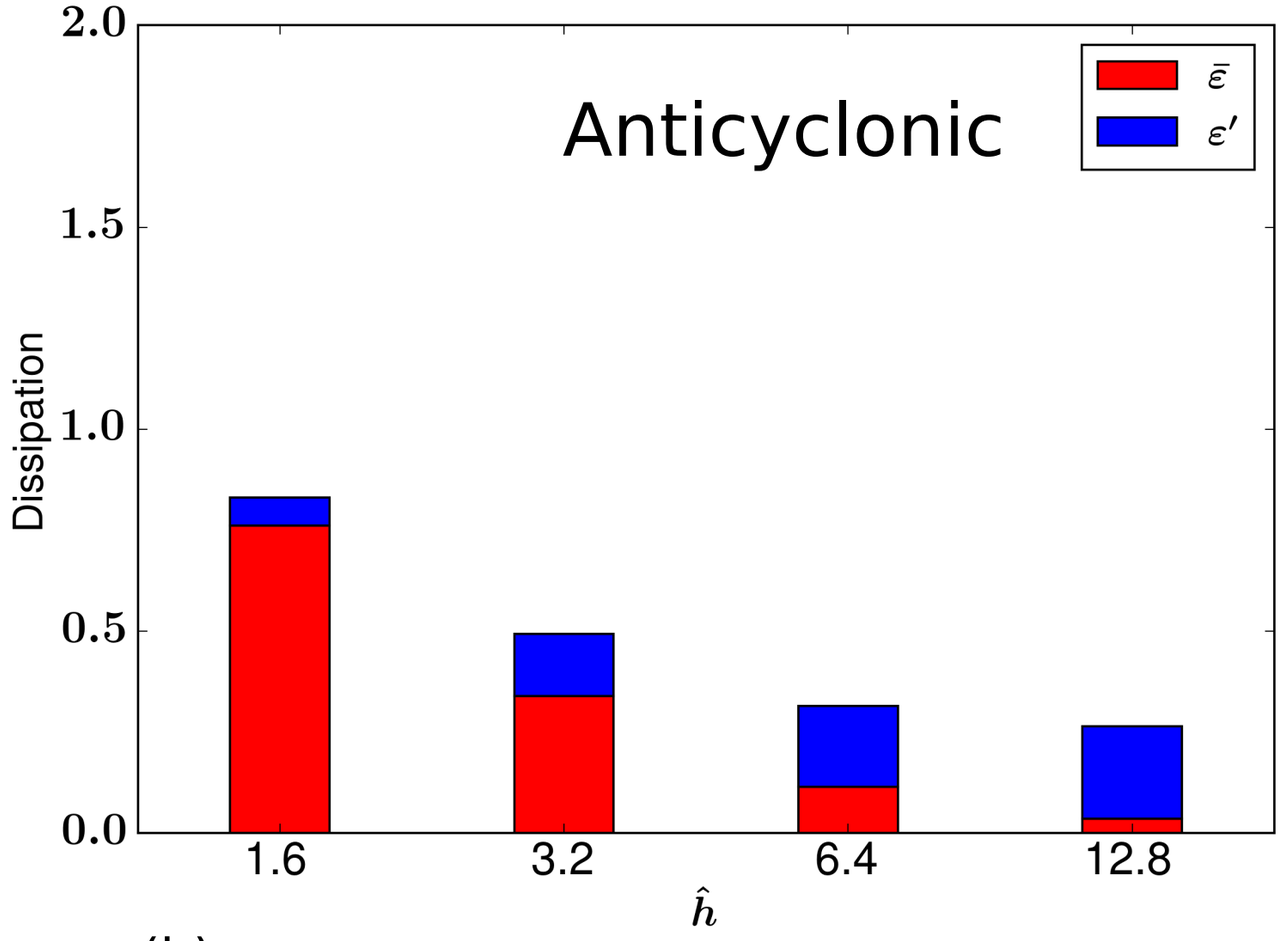
Anticyclonic
$\bar{\varepsilon}$
ε'
Dissipation
2.0
1.5
1.0
0.5
0.0
1.6
3.2
6.4
12.8
$\hat{h}$

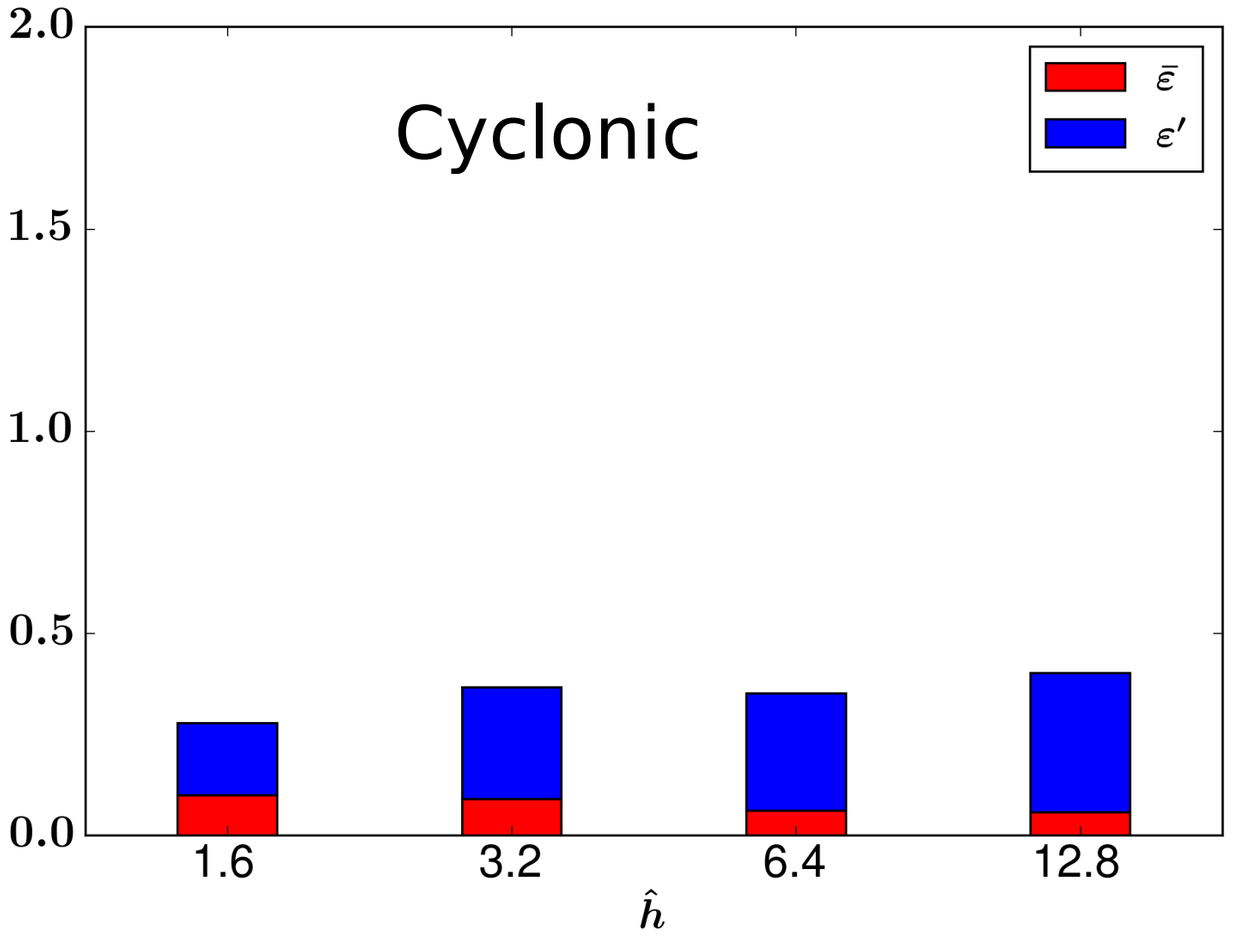
Cyclonic
$\bar{\varepsilon}$
ε'
2.0
1.5
1.0
0.5
0.0
1.6
3.2
6.4
12.8
$\hat{h}$

(b)

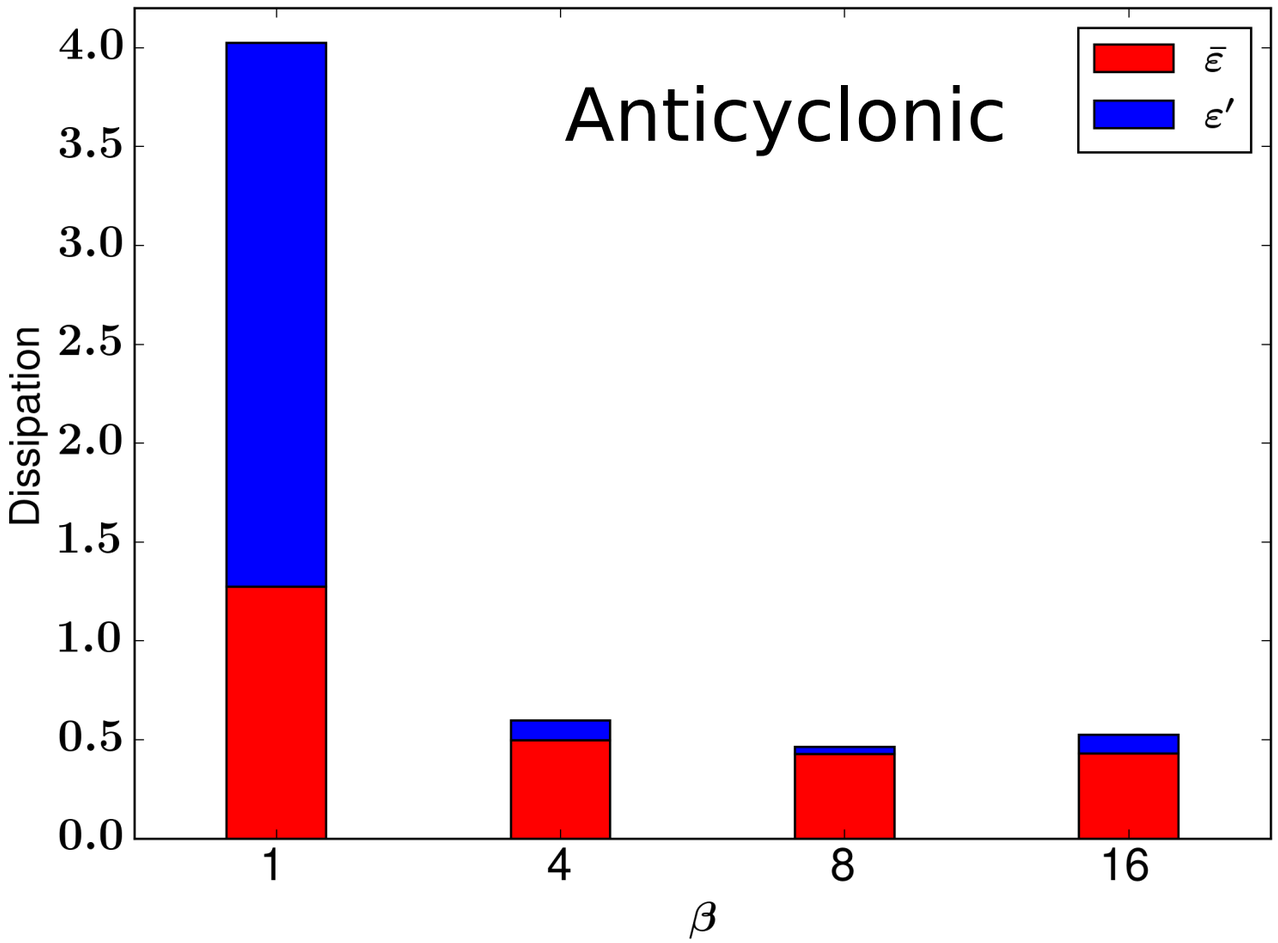
Anticyclonic
$\bar{\varepsilon}$
ε'
Dissipation
4.0
3.5
3.0
2.5
2.0
1.5
1.0
0.5
0.0
1
4
8
16
β

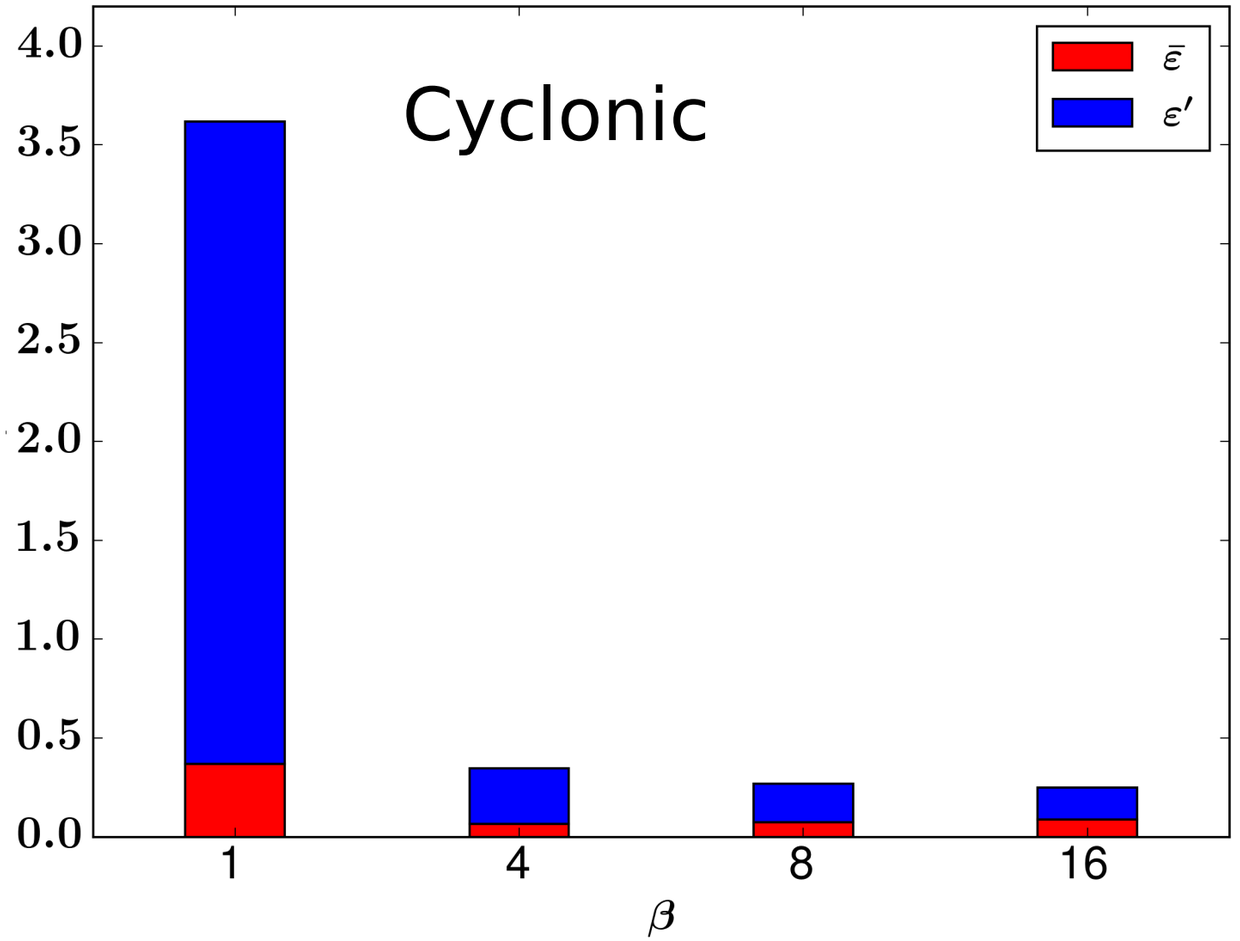
Cyclonic
$\bar{\varepsilon}$
ε'
4.0
3.5
3.0
2.5
2.0
1.5
1.0
0.5
0.0
1
4
8
16
β

Figure12.

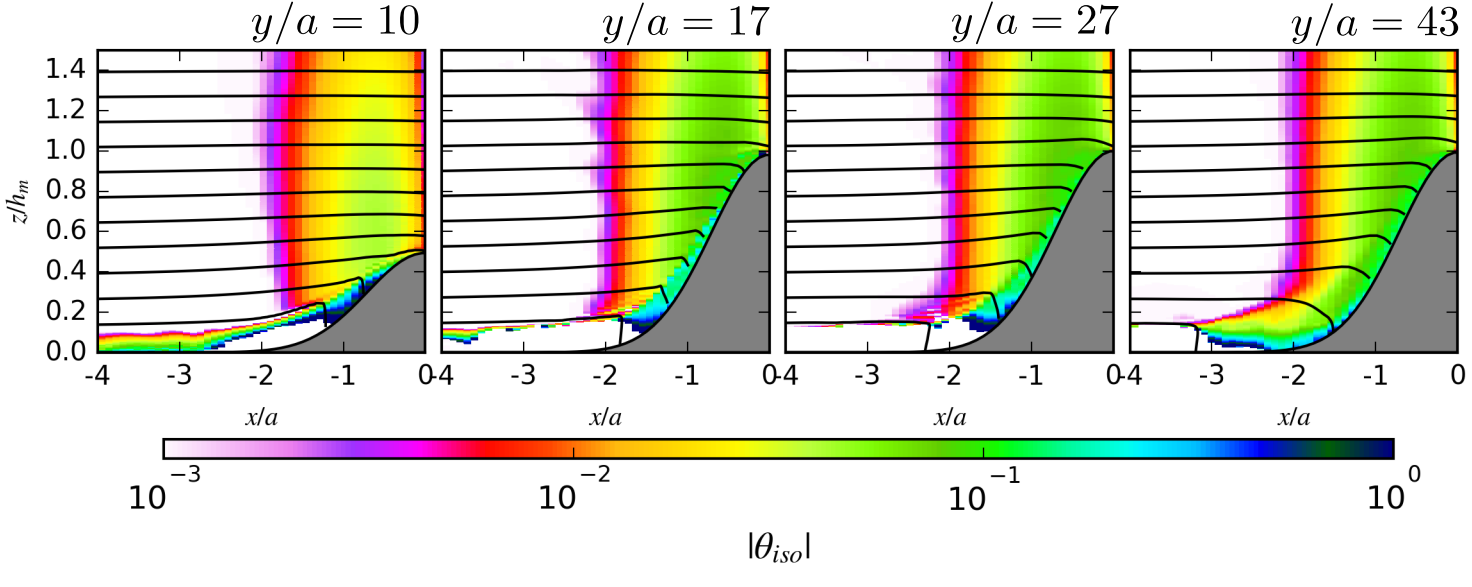
$y/a = 10$
$y/a = 17$
$y/a = 27$
$y/a = 43$
z/h_m
1.4
1.2
1.0
0.8
0.6
0.4
0.2
0.0
-4
-3
-2
-1
0
x/a
10^{-3}
10^{-2}
10^{-1}
10^{0}
$|\theta_{iso}|$

Figure13.

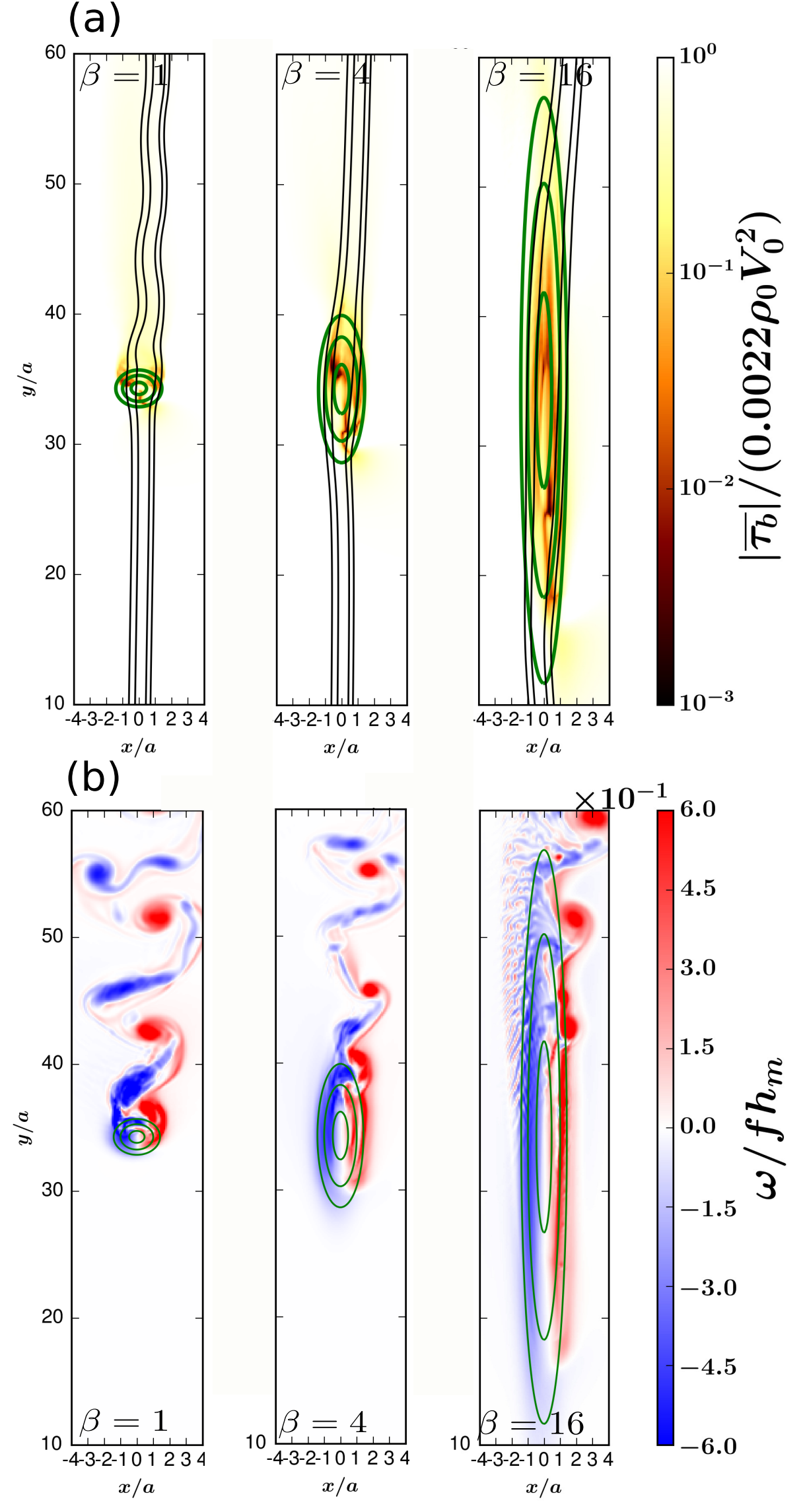
(a)
$\beta = 1$
$\beta = 4$
$\beta = 16$
y/a
x/a
$|\overline{\tau_b}|/(0.0022\rho_0 V_0^2)$
(b)
$\times 10^{-1}$
ω/fh_m
$\beta = 1$
$\beta = 4$
$\beta = 16$

Figure14.

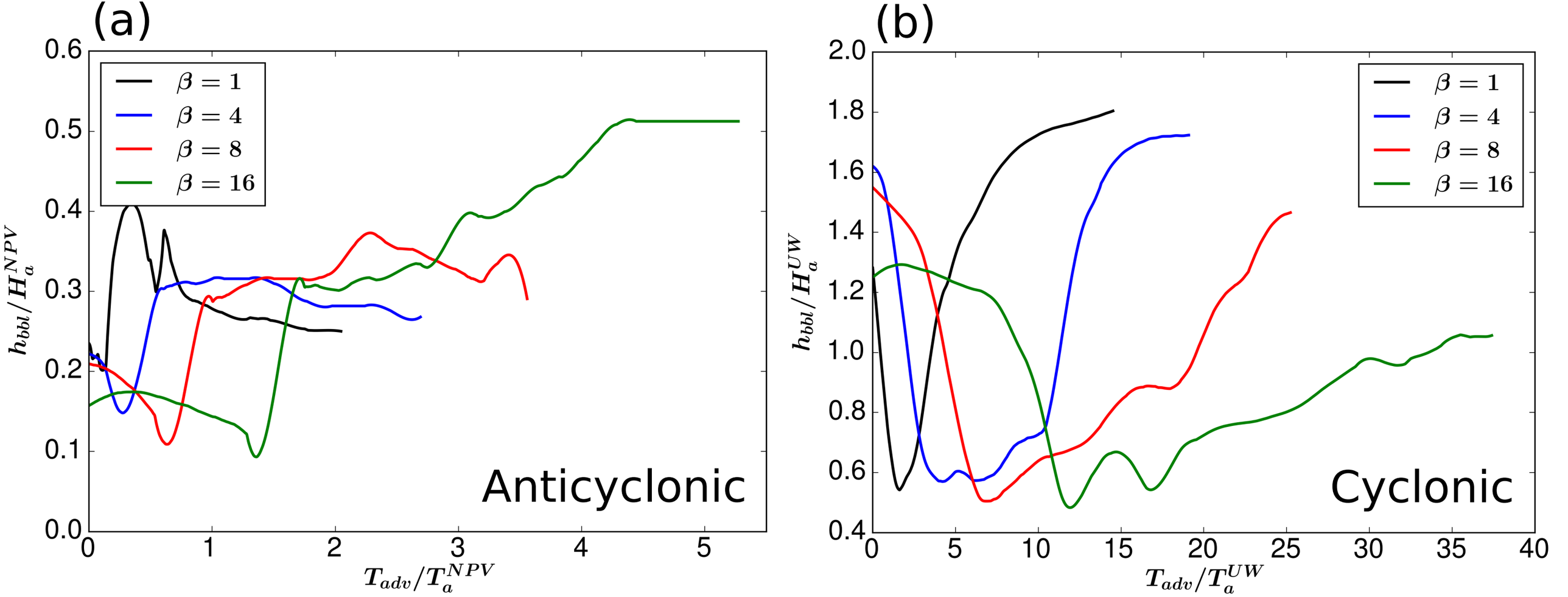
(a)
$\beta = 1$
$\beta = 4$
$\beta = 8$
$\beta = 16$
Anticyclonic
h_{bbl}/H_a^{NPV}
T_{adv}/T_a^{NPV}
0.0
0.1
0.2
0.3
0.4
0.5
0.6
0
1
2
3
4
5
(b)
$\beta = 1$
$\beta = 4$
$\beta = 8$
$\beta = 16$
Cyclonic
h_{bbl}/H_a^{UW}
T_{adv}/T_a^{UW}
0.4
0.6
0.8
1.0
1.2
1.4
1.6
1.8
2.0
0
5
10
15
20
25
30
35
40

Figure15.

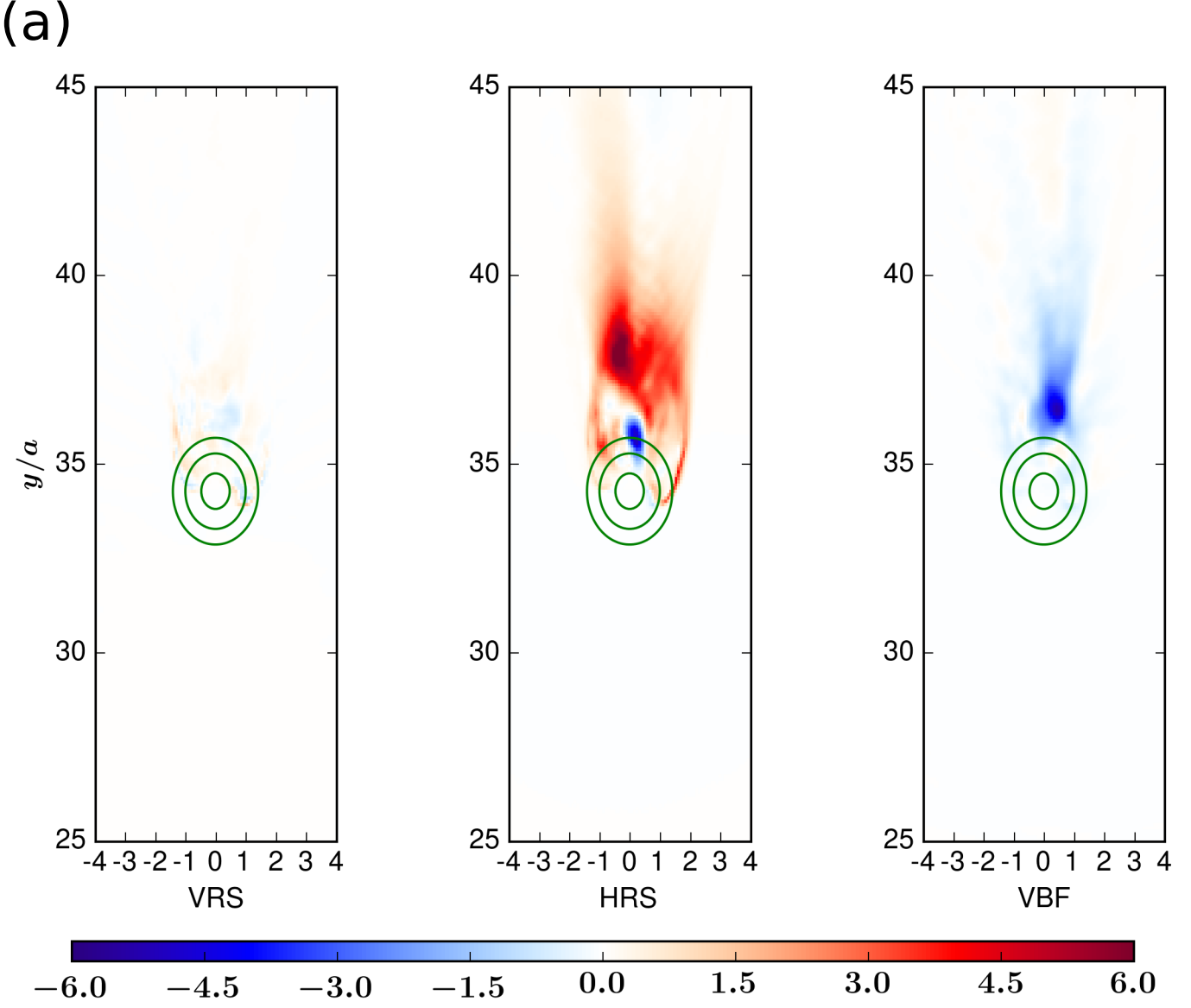
(a)
45
40
35
30
25
y/a
-4 -3 -2 -1 0 1 2 3 4
VRS
HRS
VBF
−6.0 −4.5 −3.0 −1.5 0.0 1.5 3.0 4.5 6.0

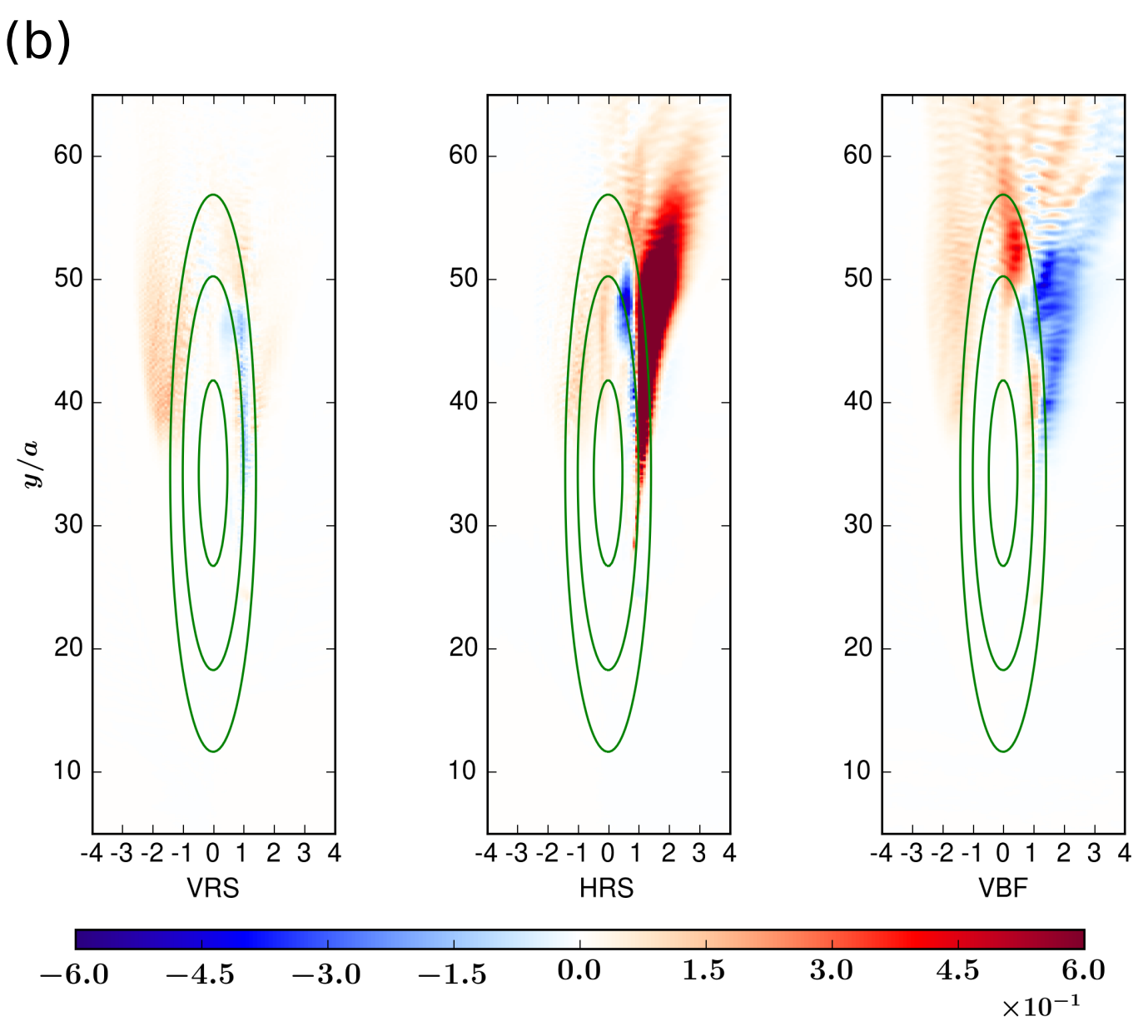
(b)
60
50
40
30
20
10
y/a
-4 -3 -2 -1 0 1 2 3 4
VRS
HRS
VBF
−6.0 −4.5 −3.0 −1.5 0.0 1.5 3.0 4.5 6.0
×10⁻¹

Figure16.

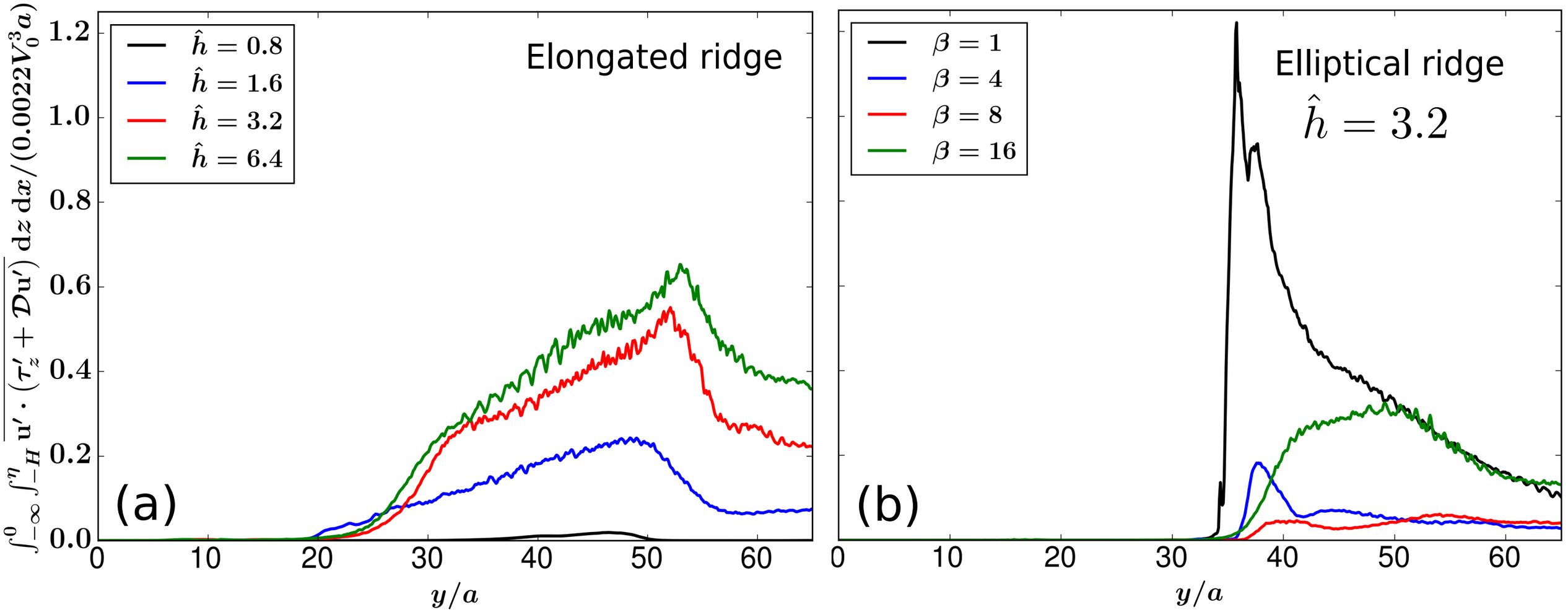
$\hat{h} = 0.8$
$\hat{h} = 1.6$
$\hat{h} = 3.2$
$\hat{h} = 6.4$
Elongated ridge
(a)
$\int_{-\infty}^{0} \int_{-H}^{\eta} \overline{\mathbf{u}' \cdot (\tau_z' + \mathcal{D}\mathbf{u}')}\, \mathrm{d}z\, \mathrm{d}x / (0.0022 V_0^3 a)$
y/a
$\beta = 1$
$\beta = 4$
$\beta = 8$
$\beta = 16$
Elliptical ridge
$\hat{h} = 3.2$
(b)
y/a